



The Unconventional Eyewall Replacement Cycle

of Hurricane Ophelia (2005)

Muhammad Naufal Razin* and Michael M. Bell

Department of Atmospheric Science, Colorado State University, Fort Collins, CO

*Corresponding author address: Muhammad Naufal Razin, Department of Atmospheric Science, Colorado State University, 3915 W. Laporte Ave., Fort Collins, CO 80521.

E-mail: naufal@colostate.edu

Early Online Release: This preliminary version has been accepted for publication in *Monthly Weather Review*, may be fully cited, and has been assigned DOI 10.1175/MWR-D-20-0181.1. The final typeset copyedited article will replace the EOR at the above DOI when it is published.

ABSTRACT

Hurricane Ophelia (2005) underwent an unconventional eyewall replacement cycle (ERC) as it was a Category 1 storm located over cold sea surface temperatures near 23°C. The ERC was analyzed using airborne radar, flight-level, and dropsonde data collected during the Hurricane Rainband and Intensity Change Experiment (RAINEX) intensive observation period on 11 September 2005. Results showed that the spin-up of the secondary tangential wind maximum during the ERC can be attributed to the efficient convergence of absolute angular momentum by the mid-level inflow of Ophelia's dominantly stratiform rainbands. This secondary tangential wind maximum strongly contributed to the azimuthal mean tangential wind field, which is conducive for increased low-level supergradient winds and corresponding outflow. The low-level supergradient forcing enhanced convergence to form a secondary eyewall. Ophelia provides a unique example of an ERC occurring in a weaker storm with predominantly stratiform rainbands, suggesting an important role of stratiform precipitation processes in the development of secondary eyewalls.

1. Introduction

Tropical cyclones (TC) have the potential to cause massive loss of life and inflict tremendous damage to infrastructure. The ability to better forecast TCs will help reduce their impacts by improving the lead time to take action prior to a TC landfall. Over the past 20 years, significant improvements have been made in TC forecasts, with notable strides made particularly in TC track forecasts. While there have also been more modest yet statistically significant improvements in TC intensity forecasts, improvements in the short-term (24-hour forecast period) TC intensity forecasts have been marginal (DeMaria et al. 2014). One of the reasons behind the difficulty in short-term TC intensity forecasts can be attributed to the challenge in predicting the onset of an eyewall replacement cycle (ERC), which can result in large intensity changes.

Using individual radial passes of aircraft reconnaissance flights into hurricanes that undergo ERCs, Sitkowski et al. (2011) classified canonical ERC events into three phases: intensification, weakening, and re-intensification. During the intensification phase, the TC inner core primary tangential wind maximum intensifies while a secondary tangential wind maximum forms and intensifies in the TC outer core. The intensification phase continues as the radii of both wind maxima contract. The weakening phase is marked by the weakening of the primary wind maximum as the radius of the secondary wind maximum continues to contract and ends when the secondary wind maximum intensity surpasses the primary wind maximum intensity. In the re-intensification phase, the new primary wind maximum associated with the outer eyewall continues to intensify and determines the storm's wind intensity. While these stages represent the canonical ERC evolution, individual storms may not undergo each stage exactly, and some may fail to reintensify. The tangential wind evolution of a canonical ERC is often accompanied by (i) the formation and contraction of a secondary eyewall associated with the strengthening and contraction of the secondary

wind maximum, and (ii) the dissipation of the primary eyewall associated with the dissipation of the primary wind maximum. As these two processes overlap, they may form concentric eyewalls that can easily be distinguished in satellite microwave imagery. Sitkowski et al. (2011) noted that the presence of the secondary wind maximum at flight level always precedes the observation of concentric eyewalls in the satellite microwave imagery, which suggests that the formation of a secondary wind maximum is a precursor to the formation of secondary eyewalls.

Smith et al. (2009) proposed that the broadening of a TC's tangential wind field through the spin-up of the outer core primary circulation can be achieved by the radial convergence of absolute angular momentum M above the boundary layer, where M is materially conserved in the absence of friction (their first mechanism). This radial convergence of M is accomplished through radial inflow in the middle troposphere in response to middle-to-upper tropospheric heating in the inner core region, as proposed by Smith et al. (2009), or in the region immediately outside of the TC inner core as proposed by Fudeyasu and Wang (2011). While Smith et al. (2009) did not frame their results in the context of an ERC, the location where the secondary tangential wind maximum occurs prior to an ERC suggests that TC rainbands located outside of the TC inner core may facilitate the broadening of the TC wind field and the formation of a secondary wind maximum prior to an ERC. Therefore, understanding the dynamics of TC rainbands may be crucial in understanding the processes behind ERCs.

TC rainbands are bands of precipitation that typically exist in a spiral geometry radially outside the TC eyewall (Willoughby et al. 1984; Houze 2010). The principal rainband is the most prominent TC rainband and it typically remains quasi-stationary relative to the translating storm center. Precipitation in the upwind portion of TC rainbands are typically dominated by deep convection, which transition into predominantly stratiform precipitation in the downwind portion of the rainbands. The distribution of precipitation in TC rainbands is also influenced by the large-

scale environment around the storm. In particular, the vertical shear of the horizontal wind of the large-scale environment strongly influences the azimuthal distribution of precipitation in TC rainbands, with convective precipitation typically found in the right-of-shear quadrants and stratiform precipitation typically found in the left-of-shear quadrants (Hence and Houze 2012).

The upwind, convective portion of TC rainbands can be characterized by three secondary circulation patterns that occur in three dimensions: (i) low-level inflow that turns upward at the base and outward near the top of the convective cells, (ii) low-level downdrafts that originate from radially outside the convective cells, and (iii) downdrafts located on the inner edge of the convective cells (Barnes et al. 1983; Hence and Houze 2008; Didlake and Houze 2009). In the azimuthal direction, convective cells are often accompanied by a convective-scale tangential wind maximum termed the secondary horizontal wind maximum (SHWM) by Samsry and Zipser (1995). The SHWM is often collocated with a convective core and can be found anywhere in the low- to mid-levels. Hence and Houze (2008) hypothesized that the strengthening of the SHWM may make the rainband more robust and, through vortex Rossby wave dynamics discussed by Montgomery and Kallenbach (1997), may help to form a secondary eyewall.

Kinematics of downwind stratiform rainbands can generally be characterized by descending mid-level inflow produced by the generation of horizontal vorticity that arises from the radial gradient of buoyancy (Didlake and Houze 2013b). Rising outflow can be found above and beneath this mid-level inflow. Through the advection of angular momentum, this mid-level inflow produces a persistent mid-level tangential jet that is of a different origin compared to that of the SHWM found in the upwind convective portion of TC rainbands. The SHWM is induced by convective-scale motions and can occur anywhere in the low- to mid-levels, whereas the tangential jets that occur in stratiform rainbands are a part of the larger mesoscale motion and occur consistently in the mid-levels due to ice microphysical processes. This stratiform mid-level tangential jet could

potentially lead to the expansion of the TC tangential wind field and serve as a precursor to an ERC.

More recent studies have linked dominantly-stratiform rainbands to the formation of secondary eyewalls in ERCs. Wunsch and Didlake (2018) built on the work of Sitkowski et al. (2011) and showed that the expansion of the wind field prior to the formation of the secondary eyewall was initiated in the downshear quadrants, with an enhancement of angular momentum in the downshear left quadrant. A similar expansion of the wind field in the downshear quadrants was found in the ERC of Hurricane Bonnie (1998) (Dougherty et al. 2018). Wunsch and Didlake (2018) attributed this enhancement of angular momentum to the convergence of high angular momentum air by the mid-level inflow of the dominantly stratiform rainbands typically found in that quadrant. Their results are consistent with the findings of Didlake et al. (2018), who also showed that this mid-level inflow, which they termed the mesoscale descending inflow, converged in the boundary layer and created persistent updraft on its inner edge which later formed the secondary eyewall in the ERC of Hurricane Earl (2010). The secondary eyewall formation mechanism proposed by Didlake et al. (2018) is corroborated by Fischer et al. (2020), who showed the same process occurring in the first of the two consecutive ERCs of Hurricane Irma (2017). Fischer et al. (2020) attributed the second ERC of Hurricane Irma to lower-tropospheric convergence between the low-level inflow and a presumed supergradient outflow. The convergence of a supergradient outflow and the low-level inflow have also been attributed to the formation of secondary eyewalls in other storms, such as Typhoon Sinlaku (Huang et al. 2012).

ERCs are relatively common in strong TCs (Kossin and Sitkowski 2009), but in this study we analyze Hurricane Ophelia (2005) as it underwent an ‘unconventional’ ERC. We characterize Ophelia’s ERC as unconventional because it occurred despite the lack of concentric eyewalls made up of deep convection, while the storm was at Category 1 intensity, and over cold sea surface tem-

peratures (SSTs). At nearly 23°C , the SSTs were approximately three degrees Celsius lower than the conventional threshold of 26.5°C that is necessary for TC genesis and sustenance (Dare and McBride 2011). Airborne radar observations of Hurricane Ophelia from the Hurricane Rainband and Intensity Change Experiment (RAINEX) field campaign will be presented herein to demonstrate that the ERC was linked to the predominantly stratiform portion of its rainbands. While observations of the more canonical ERC of Hurricane Rita (2005) from RAINEX have been analyzed previously (Houze et al. 2007; Bell et al. 2012b; Guimond et al. 2018), the observations of Ophelia's ERC have received less attention. The observations suggest that mid-level inflow associated with the dominantly stratiform rainbands broadened the TC tangential wind field through strong convergence of absolute angular momentum above the boundary layer. Flight-level and dropsonde analysis will show that the local maximum within the broadened tangential wind field produced supergradient winds, which resulted in the formation of a secondary eyewall through enhanced convergence with the storm inflow.

Guided by the findings of aforementioned studies on TC rainbands and their potential influence on the formation of a secondary wind maximum prior to an ERC, the role of rainband precipitation in the ERC of Hurricane Ophelia (2005) was investigated using the RAINEX airborne radar, flight-level and dropsonde datasets, and a spline-based variational wind synthesis tool. The different datasets and the analysis technique employed will be discussed in Section 2. The evolution of Hurricane Ophelia throughout its lifetime and the results from the rainband analyses are discussed in Section 3, while a momentum budget analysis is discussed in Section 4. An axisymmetric view of the rainband dynamics and a hypothesized ERC mechanism are provided in Section 5, with concluding remarks in Section 6.

2. Data & Methods

The airborne radar dataset used in this study is from the Hurricane Rainband and Intensity Change Experiment (RAINEX) in 2005 (Houze et al. 2006). The goal of RAINEX was to utilize a high-resolution numerical weather model alongside aircraft observations to investigate the roles of eyewalls and rainbands in influencing TC intensity change. The study herein utilizes radar observations made in Hurricane Ophelia on 11 September 2005 by the Naval Research Laboratory (NRL) and one of the two NOAA P-3 (hereafter N43) aircraft.

N43 was equipped with a single-parabolic antenna which alternately scans fore and aft to achieve pseudo-dual Doppler measurements (Jorgensen et al. 1996). The scanning results in an along-track sampling resolution of approximately 1.5 km. The NRL P-3 was equipped with the National Center for Atmospheric Research (NCAR) dual-beam Electra Doppler Radar (ELDORA; Hildebrand et al. 1996), which has an along-track sampling resolution of about 0.4 km. One of the sampling strategies employed by RAINEX was to make “quad-Doppler” measurements of the rainbands. The strategy involved two aircraft flying on either side of the rainband and simultaneously sampling the wind components inside the rainband, thus producing the most reliable wind estimates (Jorgensen et al. 1996).

On 11 September 2005, there were four periods during which N43 and NRL were simultaneously sampling Ophelia’s rainbands - allowing for quad-Doppler wind retrievals. These four periods were then categorized into four rainband “sectors.” The locations of these rainband sectors relative to the storm center are shown in Figure 1, while the observation periods for all four rainband sectors are listed in Table 1. We denote the dominantly convective sector of Ophelia’s rainbands as “rainband-C”, the dominantly stratiform sectors as “rainband-S1” and “rainband-S2”, and the sector that we hypothesize to be the developing secondary eyewall as “DSE”. Rainband-S1

and rainband-S2 are two consecutive observation periods of Ophelia's dominantly stratiform rainband and largely overlap in space. Our analyses showed that they have the same characteristics and therefore support the same scientific conclusions, such that only the results from rainband-S2 will be discussed in detail. A cross-section from each of the four rainband sectors will be shown for completeness.

The airborne radar data was first corrected for navigational errors (Testud et al. 1995) and initially quality controlled (QC) to remove non-meteorological echoes and instrument noise using the 'medium' QC algorithm from Bell et al. (2013). Any remaining non-meteorological echoes and noise were then manually removed using NCAR's Solo II software (Bell et al. 2013). In order to correctly apply a convective-stratiform partitioning algorithm (Didlake and Houze 2009), a low bias in the N43 reflectivity field needed to be corrected. Using the ELDORA reflectivity field as reference, a constant bias correction of 7.87 dBZ was added to the N43 reflectivity field. Details of the correction methodology can be found in Razin (2018).

Hurricane Ophelia's track and intensity are obtained from the best-track dataset (Jarvinen et al. 1984; McAdie et al. 2009; Landsea and Franklin 2013), while information on the environmental shear around Ophelia throughout its lifetime are obtained from the Statistical Hurricane Intensity Prediction Scheme dataset (SHIPS; DeMaria et al. 2005). The environmental shear variables used for this study are the direction (degree heading) and magnitude (m s^{-1}) of the 850 to 200 hPa shear over an annulus of 0 to 500 km from the 850 hPa vortex center (SDDC and SHDC fields). The SDDC and SHDC were calculated from the Global Forecast System winds with the vortex removed. Both the best-track dataset and the SHIPS dataset were obtained from The Enhanced Vortex Data Message Dataset (VDM+) compiled by Vigh (2015).

To show the evolution of the daily sea surface temperature (SST) around Hurricane Ophelia from the 9th to the 14th, the Daily Optimum Interpolation Sea Surface Temperature (OISST) dataset

from the National Oceanic and Atmospheric Administration (NOAA) National Centers for Environmental Information (NCEI) was used. The OISST blends observations from satellites, ships, and buoys to provide a spatially complete SST map at 0.25 degree spatial resolution (Banzon et al. 2016).

The evolution of Ophelia's tangential wind field was analyzed using flight-level data from the United States Air Force (USAF) aircraft reconnaissance missions. The flight-level data were obtained from FLIGHT+: The Extended Flight Level Dataset for Tropical Cyclones (Version 1.1; Vigh et al. 2016). In a typical hurricane aircraft reconnaissance mission, the aircraft would fly multiple radial paths that transect the center of the TC, providing radial profiles of flight-level dynamic and thermodynamic variables in different quadrants of the storm. Each flight track towards or away from the center of the TC is considered as one radial leg. The USAF C-130 aircraft flew at the 700 mb level in nine reconnaissance flights into Hurricane Ophelia, with a minimum number of six radial legs in each mission. For each mission, the radial profile of the tangential wind was azimuthally averaged and then smoothed using a 10-km low-pass Lanczos filter.

To complement the flight-level dataset, microwave imagery of Hurricane Ophelia were obtained from the Naval Research Laboratory Tropical Cyclones website (NRL 2005). The microwave sensors from which these images are retrieved are aboard polar-orbiting satellites which provide only a snapshot of the storm at a particular time. When available, the image closest to the time of each aircraft reconnaissance mission was selected, providing a corresponding satellite image for six of the nine aircraft reconnaissance missions. Satellite microwave imagery around the time the research flights were conducted were also retrieved, providing one image around the start of the research flight and two images after the conclusion of the research flights.

The images obtained are the horizontally-polarized 85-, 89-, 91-, and 37-GHz channels from Defense Meteorological Satellite Program's (DMSP) F-12, F-13, F-14 and F-16 satellites, the

Tropical Rainfall Measuring Mission (TRMM) satellite, and NASA’s Aqua-1 satellite. Low/cold brightness temperatures in the 85- to 91-GHz channels associated with scattering of terrestrial radiation by precipitation-sized ice particles serve as a proxy for the location of deep convection, providing an estimate of the distribution of convection in the storm associated with the corresponding observed flight-level tangential wind profile. In the 37-GHz channel, low-level “warm clouds” and rain appear as warm brightness temperatures compared to the ocean surface. The radiation detected in this channel is insensitive to scattering by small ice particles above them. Thus, an image of the low-level cloud and precipitation fields associated with shallow convection can be retrieved, even if they occurred underneath the TC cirrus shield. A gridded satellite visible image of Hurricane Ophelia at 2100 UTC is shown in Fig. 1 (GRIDSAT; Knapp and Wilkins 2018) to provide a reference image of the storm-relative flight track for the observation period that began at 1853 UTC and ended at 2210 UTC on 11 September 2005.

Three-dimensional quad-Doppler analysis of each leg was done using a spline-based variational wind synthesis tool known as SAMURAI (Bell et al. 2012a; Foerster et al. 2014). The analysis domain was centered at the center of the storm. Ophelia moved very little on the day the observations were made. Therefore, the storm motion was assumed to be stationary, with the storm centered at 31.39°N 75.94°W . The storm center used for the analysis is based on a combination of best-track, aircraft center fixes, and the radar reflectivity field. The analysis was conducted on a Cartesian f-plane with a horizontal resolution of 1 km and a vertical resolution of 0.5 km. Though much of analysis domain has quad-Doppler coverage, the curved nature of the aircraft flight tracks can still result in some regions where the radar beam geometry is sub-optimal. The quality of the wind solution throughout the domain was assessed by the condition number of a multi-Doppler geometry matrix inversion using the Fast Reorder And CEDRIC Technique in the Lidar Radar Open Software Environment (FRACTL, Bell et al. 2020). Regions with high condition numbers

and poor wind quality were removed from the analysis. The analysis fields were then interpolated onto cylindrical coordinates with 1 degree azimuthal resolution and 1 km radial resolution. Sector averages were subsequently calculated, with a minimum azimuthal fraction of data above 20% along each radii required for analysis.

3. Results

a. Hurricane Ophelia (2005)

The track and intensity evolution of Hurricane Ophelia are summarized briefly here from a more detailed discussion by Beven and Cobb (2006). The best-track center position and intensity of the TC are shown in Fig. 2 and Fig. 3, respectively. Ophelia was classified as a tropical depression at around 0600 UTC 6 September and proceeded on a northward track before becoming a tropical storm around 0600 UTC 7 September. Tropical Storm Ophelia intensified steadily as it made a counter-clockwise loop off the Florida east coast between 1800 UTC 7 September and 0000 UTC 9 September, where it briefly became a Category 1 hurricane. It was downgraded back to a tropical storm by 0600 UTC 9 September. By 1800 UTC 9 September, Ophelia became a Category 1 hurricane again as it moved out into the open ocean and away from land, only to be downgraded to a tropical storm again six hours later.

As Ophelia became a Category 1 hurricane for the third time in its lifetime at 1200 UTC 10 September, it was making a slow clockwise loop. Between 1800 UTC 10 September and 1800 UTC 11 September, the storm was relatively stationary. At this point, Hurricane Ophelia was located over cold ocean water that was upwelled due to its own wind field. The daily average sea surface temperature (SST) over which Ophelia was located was as cold as 23.5°C (Fig. 4c), significantly below the theoretical threshold of approximately 26.5°C needed for TC genesis and

sustenance (Dare and McBride 2011). By 0000 UTC 12 September, Ophelia was a tropical storm again. It remained at that intensity as it continued moving up along the east coast of the United States, becoming a Category 1 hurricane for a fourth time at 0000 UTC 14 September. Ophelia reached its peak intensity of 75 knots for the second time at 1200 UTC 14 September, not long before it made its closest approach to land. However, hurricane-force winds remained offshore. By 0000 UTC 16 September, Ophelia weakened into a tropical storm for the last time as it accelerated northeastward, underwent extratropical transition at 0000 UTC 18 September, and dissipated by 0600 UTC 23 September.

b. Flight-Level Tangential Wind Evolution

The evolution of Ophelia's azimuthal mean tangential wind field as observed by nine aircraft reconnaissance missions is shown in Fig. 5 and the corresponding satellite microwave imagery for six of these missions are shown in Fig. 6. During the first mission at 1130 UTC 10 September, the flight-level tangential winds were characterized by a single peak of about 34 m s^{-1} (primary wind maximum), with a radius of maximum wind (RMW) at about 50 km. The radial profile and best-track data indicate that Ophelia was a Category 1 hurricane that was slowly intensifying at this time (Fig. 3). Satellite microwave imagery at around the same time show that Ophelia's eyewall had strong convection located on the northern periphery of the eye at about the same distance as the RMW (Fig. 6a). Convection associated with an inner rainband was evident just outside the eyewall and spiraling outward from the northeast to the southwest. This rainband was twice sampled by the aircraft. Examination of the individual passes indicate that a secondary wind maximum was not present at flight level (not shown), but the existence of a secondary wind maximum at other vertical levels cannot be ruled out.

By 2245 UTC 10 September, Ophelia’s tangential wind had strengthened slightly while its RMW had also contracted slightly (Fig. 5). The northern portion of Ophelia’s eyewall remained convectively active around the RMW, while the southern portion of the eyewall appeared “broken” with no apparent deep convection (Fig. 6b). In addition, the convection in the inner rainband had weakened significantly. Shortly after this flight, the center was nearly stationary and became located over the colder SSTs due to upwelling. We hypothesize that the inner eyewall dissipated during this period due to the lack of sufficient surface enthalpy fluxes near the center, but that slightly warmer SSTs radially outward were still able to support relatively weak convection (c.f. Fig. 4c). Though detailed observations are not available until the end this period, the hypothesis is consistent with results from coupled simulations of the storm evolution that show reduced air-sea fluxes due to the upwelling (Smith 2016).

At 0030 UTC 12 September, Ophelia’s primary wind maximum had weakened, and there was a secondary wind maximum of about 31 m s^{-1} at a radius of 95 km from the center of the storm. Consistent with the flight-level tangential wind profile, satellite microwave imagery showed convection in Ophelia’s eyewall had dissipated (Fig. 6c). Instead, there were two bands of convection associated with one or possibly more rainbands. The inner band of convection spiraled outward from the north to the east, while the outer band of convection spiraled outward from the northeast to the south. At this time, Ophelia had just weakened back to a tropical storm (Fig. 3).

At 2300 UTC 12 September, the primary wind maximum had completely dissipated and the secondary wind maximum at a radius of 102 km had become the new wind maximum. Concurrently, Ophelia’s eye had gotten larger as it was surrounded by a near-circular band of convection, with stronger convection to the south and weaker convection to the north (Fig. 6d). At this time, Ophelia’s intensity was at a relative minimum (Fig. 3). At 2030 UTC 13 September, Ophelia was re-intensifying and was moving away from colder SSTs over into warmer SSTs (Fig. 4c,d), while

its RMW had contracted to a radius of 89 km. Associated with the warmer SSTs, a region of convection can be seen on the northern periphery of the eye around 33°N 78°W (Fig. 6e). However, this eyewall convection was relatively small and was located too close to the center of the storm to be associated with the corresponding flight-level tangential wind maximum farther out, indicating that inner core convection was just beginning to be re-invigorated. Ophelia's rainbands also appeared to have assumed its original spiral structure. By 2315 UTC 14 September, Ophelia's RMW had contracted to a radius of 63 km, with eyewall convection surrounding the eye at approximately the same radius.

The foregoing discussion on the evolution of Ophelia's azimuthal mean tangential wind field and the eyewall and rainband convection shows a typical progression of an ERC. However, the satellite microwave imagery showed that Ophelia's ERC did not involve concentric rings of deep convection associated with closed concentric eyewalls. Comparing the schematic of ERC progression by Sitkowski et al. (2011) (their Fig. 8) to the observed flight-level tangential wind evolution, Ophelia's intensification and weakening phases occurred between 2245 UTC 10 September and 0030 UTC 12 September, and its re-intensification phase occurred around 0030 UTC 12 September. We would like to note however, that our analysis is based on the azimuthal mean tangential wind field, while the analysis done by Sitkowski et al. (2011) is based on individual radial passes. While ERCs are fairly common in major TCs (Category 3 or stronger), ERCs in a Category 1 TC such as Ophelia are rare. Only 5% of the 45 secondary eyewall formation events in the North Atlantic between 1997 and 2006 occurred in Category 1 storms (Kossin and Sitkowski 2009). However, these storms did not necessarily undergo a complete ERC. Nevertheless, Ophelia exhibited all the common features typically associated with canonical ERCs as discussed from the evolution of its intensity and flight-level tangential wind profiles.

c. Rainband Analysis

Since ERCs typically occur in major hurricanes and involve concentric deep convective eye-walls, Ophelia's ERC proved to be unconventional as it occurred when the storm was at Category 1 intensity, located over cold SSTs, and lacked the presence of closed concentric eyewalls made up of deep convection. An analysis of RAINEX airborne radar observations of the rainbands of Hurricane Ophelia was conducted to provide insight into the mechanisms that are responsible for this unconventional ERC. Quad-Doppler analyses were conducted for the different sectors of Ophelia's rainbands as labeled in Table 1, with the approximate observation period highlighted by the hatched line in Fig. 3. For reference, the 0-500 km shear at 1800 UTC 11 September had a heading of 79° (east-northeast) and a magnitude of 6.2 m s^{-1} , and is represented by the arrow in Fig. 1.

1) DOMINANTLY CONVECTIVE RAINBANDS (RAINBAND-C)

Rainband-C is located in the downshear quadrants of the storm, with a slightly bigger portion being in the right-of-shear quadrant (Fig. 1). This region is where the most vigorous convection and heavier precipitation are expected (Hence and Houze 2012). Convection in rainband-C is loosely organized into two bands that spiral in along with the rainband (Fig. 1b). Averages of the reflectivity field, radial, tangential and vertical velocities in rainband-C were calculated for the sector shown in Fig. 1b and are shown in Fig. 7. Rainband-C is generally populated by shallow convection, with the 20 dBZ average reflectivity contour reaching up to an altitude of only 6 km (Fig. 7d). A closer inspection reveals two distinct regions of convection: the “inner” region between 70 - 150 km radius, and the “outer” region between 150 - 200 km radius. Each region is marked by two columns of local reflectivity maximum that are denoted by the 30 dBZ reflectivity contour. The collocation of a local low-level convergence maximum and upper-level

divergence maximum with these reflectivity columns in individual cross-sections indicate that they are associated with convective updrafts (not shown).

The inner region is dominated by shallower reflectivity columns that reach an average altitude of about 4 km, whereas the outer region is dominated by deeper reflectivity columns that reach an average altitude of 5 km. The enhancements in the 20 dBZ contours in the outer region indicate the presence of deeper convection within the rainband. The shallow rainband convection and decreasing convective heights with decreasing radius has been well documented (Hence and Houze 2012; Didlake and Houze 2013a). This configuration of rainband convection has been attributed to the vertical shear of the horizontal winds produced by eyewall outflow that acts to limit the vertical extent of convection. The deeper convection observed in the outer region of rainband-C is associated with the eyewall outflow's weakening influence in limiting the vertical extent of rainband convection. Radial variations in buoyancy also play a role in determining the depth of the convection.

The secondary circulation was characterized by a low-level inflow and an upper-level outflow, typical of that seen in dominantly convective rainbands (Hence and Houze 2008). Similar to the observations made by Didlake and Houze (2013a), the depth of the radial inflow (denoted here simply by regions negative radial velocities) decreases at smaller radii, with the inflow layer reaching up to an altitude of 4 km in the outer region and 2 km in the inner region (Fig. 7b). An updraft and an outflow maximum is seen above each convective column in the inner region, with the outflow layer decreasing in height radially inside the inner region. The updraft and outflow in the outer region are less apparent in this sector-averaged view (Fig. 7a,b). There is a tangential wind maximum in the inner convective column of the inner region, just above the inflow layer at 1.5 km altitude (Fig. 7c). This tangential jet appears disorganized, occupies only a small portion of the leg, and is significantly weaker at 4 km altitude. There is also a local but weak tangential

wind maximum associated with the convective columns in the outer region, located at around 3 km altitude.

Observations in rainband-C corroborate some of the observations made by Didlake and Houze (2013a) in a similar dominantly convective rainband of Hurricane Rita (2005). The height of convection and the depth of the inflow layer decreases at smaller radii. There is also a low-level tangential jet associated with the convective column in the inner region. In contrast to the findings of Didlake and Houze (2013a), there is no distinguishable difference in the strength of the inflow between the inner region and the outer region. However, the radar analysis cannot accurately resolve the winds below 500 m altitude, where radial differences in inflow strength could exist. The difference between the convective rainbands of Ophelia and Rita may be indicative of structural difference between storms of different intensities, since Ophelia was a weakening Category 1 storm at the time of the observation while Rita was an intensifying Category 5 storm. Nonetheless, the structure of the sector-averaged variables in rainband-C is generally consistent with the conceptual model of a dominantly convective portion of a TC rainband.

2) DOMINANTLY STRATIFORM RAINBAND (RAINBAND-S2)

Analysis of rainband-S2 (Fig. 1) indicates that double-band convection feature seen in rainband-C has continued, but the convection is organized in quasi-linear configuration with stratiform precipitation located in between the two bands of convection (Fig. 1b). In the outer region of rainband-S2, convective-classified echoes are dominant in the upwind portion of the rainband and become diminished towards the downwind end. In contrast, convective echoes in the inner region are weaker in the upwind end and stronger in the downwind end.

In a shear-relative framework, stratiform precipitation is expected to be dominant in the left-of-shear and upshear quadrants (Hence and Houze 2012). However, rainband-S2 can still be charac-

terized by some convective-classified echoes. The convective-classified echoes in the inner region may be embedded convection, or are just an artifact of the convective-stratiform partitioning algorithm, which is based on a combination of reflectivity thresholds as well as a calculation of the horizontal gradient in reflectivity at 2 km altitude. Essentially, a location may be classified as convective if its reflectivity value is higher by a certain amount relative to its surrounding. The convective centers in the inner region, as defined by the algorithm, may simply be locally-enhanced precipitation (and therefore locally-enhanced reflectivity) that arose from the larger stratiform circulation. Didlake and Houze (2013b) associated this locally-enhanced precipitation with the rising outflow maximum of the stratiform precipitation. This rising outflow maximum can be sufficiently strong to keep precipitation particles aloft long enough for them to grow large and produce locally-enhanced reflectivity columns that resemble the reflectivity columns produced from convective updrafts.

Sector averages of the reflectivity field, radial, tangential and vertical velocities in rainband-S2 were calculated for the sector shown in Fig. 1b, and are depicted in Fig. 8. This leg is characterized by the presence of a descending mid-level inflow (Fig. 8b). This inflow, which is much shallower in depth than that observed in Hurricane Rita's rainband (Didlake and Houze 2013b), begins from radially outside the rainband where the vertical velocities are weakly positive and continues into the rainband. On the inner edge of this mid-level inflow, a tangential wind maximum can be found, centered at around 100 km radius and 2 km altitude. Strong winds of similar strength to the tangential wind maximum extend up to an altitude of 4 km (Fig. 8c). However, the whole rainband is associated with a large area of stronger tangential winds relative to rainband-C, with winds over 30 m s^{-1} present in a large portion of the rainband.

Rising outflow is found above the inner edge of the descending inflow at around 100 km radius (Fig. 8a,b), which is collocated with the top of a local reflectivity maximum. There is also another

region of rising outflow beneath the descending mid-level inflow. This structure is consistent across individual cross-sections (not shown), and it is in agreement with the observations made by Didlake and Houze (2013b) of the dominantly stratiform rainband of Hurricane Rita and with the idealized simulation of stratiform heating in the rainband by Moon and Nolan (2010). Thus, the local reflectivity maximum is most likely associated with the larger stratiform-scale circulation and not by embedded convection. The rising outflow beneath the mid-level inflow is the supergradient response to the tangential wind maximum located on its inner edge (Didlake and Houze 2013b), as will be further discussed in Section 5.

3) DEVELOPING SECONDARY EYEWALL (DSE)

The DSE is located in the right-of-shear quadrants of Ophelia (Fig. 1). The double band convection feature seen in the previous legs is absent in this leg (Fig. 1b). The inner region consists of convective-classified echoes that continue from rainband-S2. In the outer region, patches of convective echoes located south of the eye between 125 and 150 km radius spiral inward and merge with the inner region at approximately 75 km radius to the southeast of the eye. There is little variation in the population of convective-classified echoes between the upwind region and downwind region of DSE.

Sector averages of the reflectivity field, radial, tangential and vertical velocities of DSE are shown in Fig. 9. A deep layer of low-level rising inflow is observed in DSE, with the depth of the inflow layer extending up to 5 km altitude (Fig. 9b). Above this deep inflow layer, there is (i) outflow that extends up to 8 km altitude, (ii) weak inflow corresponding to remnant stratiform mid-level inflow that extends up to 10 km altitude, and (iii) strong outflow extending to the top of the analysis domain.

The corresponding tangential winds in DSE are enhanced throughout the whole rainband region, which extends up to 6 km altitude (Fig. 9c). There is a tilted region of stronger tangential winds, stretching from 70 km radius at low levels to 100 km radius at around 5 km altitude. The radial and tangential wind profiles of DSE seem to be a combination of rainband-C and rainband-S2. However, the deep inflow layer associated with the in-up-out secondary circulation, and the single convective tower located on the inner edge of the rainband indicated that this portion of the rainband is dominantly convective. Since this rainband was sampled later in time, we hypothesize that stratiform kinematics here have transitioned to a more convective kinematics that make up the developing secondary eyewall associated with Ophelia's ERC. Further discussions will be offered in later sections.

4) REPRESENTATIVE RAINBAND CROSS-SECTIONS

To support and summarize the findings of the sector-averaged analyses above, representative cross-sections of the reflectivity field and tangential and radial velocities were taken from rainband-C, rainband-S1, rainband-S2 and DSE, labeled CS-C, CS-S1, CS-S2 and CS-DSE, respectively. The locations of these representative cross-sections are shown in Fig. 1a, with their respective tangential and radial velocity fields shown in Fig. 10.

CS-C is characterized by low-level inflow, upper-level outflow, and decreasing inflow depth with decreasing radius (Fig. 10b). The largest decrease in inflow depth is collocated with local reflectivity maxima at around 165 km and 120 km radius. Where the inflow is strong, there is generally stronger tangential winds, with a tangential jet located around 120 km radius at 2 km altitude (Fig. 10a). Downwind of CS-C, CS-S1 is associated with a deep layer of strong mid-level inflow and an overall broader and stronger tangential wind field compared to CS-C (Fig. 10c,d).

Peak tangential winds can be found on the inner edge of this mid-level inflow, at around 90 km radius and below 3 km altitude.

The circulation in CS-S2 is similar to CS-S1, but with diminished magnitude of mid-level radial inflow (Fig. 10e,f). However, an overall stronger wind field relative to CS-C is still apparent, with a tangential jet still located on the inner edge of the mid-level inflow. There are hints of a shallow inflow layer in the lower levels in both CS-S1 and CS-S2, beneath the supergradient outflow. This inflow layer is likely associated with the larger storm-scale secondary circulation. Since the radar analysis cannot accurately resolve the winds below 500 m altitude, the exact nature of this inflow cannot be deduced. Further downwind of CS-S2, the circulation in CS-DSE is more similar to that in CS-C, except that the inflow seen in CS-DSE is much deeper (Fig. 10g,h). A remnant mid-level inflow can also be seen in CS-DSE, at around 130 km radius and 8 km altitude. There is also a tilted tangential wind maximum located at around 80 km radius and extends up to 5 km altitude at 100 km radius.

As shown above, the dominantly convective rainband-C and its representative cross-section CS-C are associated with localized low-level tangential wind maxima that are tied to the convective-scale circulation. However, the dominantly stratiform rainband-S1 and -S2, and their respective representative cross-sections CS-S1 and CS-S2 are associated with a broader and stronger tangential wind field and a strong low-level outflow consistent with supergradient flow. Downwind of the dominantly stratiform rainband, in DSE and its representative cross-section CS-DSE, the stratiform rainband kinematics transition back into dominantly convective kinematics. We hypothesize that DSE is the developing secondary eyewall in Ophelia's ERC. Here, we define the secondary eyewall as possessing a dominantly convective secondary circulation. Moreover, the vertical structure in the local tangential wind maximum is aligned with the reflectivity maximum in CS-DSE (Fig. 10g) and closely resembles that of a typical inner or primary eyewall seen in previous studies.

However, if we were to define the secondary eyewall as characterized by a strong tangential wind maximum, then an argument can be made that the secondary eyewall formed in the dominantly stratiform rainband-S1 and -S2. The local tangential wind maximum in rainband-S1 and -S2 are radially collocated with the secondary tangential wind maximum in Ophelia's ERC (Fig. 5). We chose not to define the secondary eyewall based solely on the tangential wind field, and instead also included the characteristic of a dominantly convective secondary circulation, due to the convective nature typically associated with a primary or secondary eyewall. Given that the DSE is directly downwind of Ophelia's dominantly stratiform rainbands, the formation of the DSE must be strongly tied to the stratiform rainband dynamics compared to that of the more distant dominantly convective rainbands. We hypothesize that the kinematics of rainband-S1, -S2, and DSE are different spatial and temporal sections in the ERC process, as will be further elaborated in Section 5.

The 85-GHz satellite microwave imagery captured around the time the research flights were conducted provide further evidence to the airborne radar observations. Just before the research flights began, deep convection was active in the outer rainbands of Hurricane Ophelia (Fig. 11a). The location of this deep convection is in the approximate location of rainband-C. Convection in rainband-S1, -S2, and DSE were weak. After the conclusion of the research flight, overall rainband convection had diminished (Fig. 11c). However, shallow convection was still present and was observed in the 37-GHz satellite microwave imagery (Fig. 11b). In the 37-GHz image, shallow eyewall convection was “opened” to the southwest of the TC center. Outside the eyewall, a moat - a relatively precipitation-free region - had formed in arc that extended from the west to the south. Radially outside of this moat are rainband-S2 and DSE. The image resembles that of a secondary eyewall made up of rainband-S2 and DSE, and serves as additional evidence for their respective roles in Ophelia's ERC.

4. Absolute Angular Momentum (AAM) Budget

To understand how the secondary circulation of Ophelia's rainbands may contribute to the spin-up of the storm's tangential winds, an absolute angular momentum (AAM) budget for each rainband leg is calculated using the flux form of the azimuthally-averaged tangential momentum equation in cylindrical coordinates. Assuming that the frictional torques are negligible, which is a reasonable approximation for the free troposphere above the TC boundary layer, the azimuthally-averaged AAM flux divergence equation can be written as:

$$\frac{\partial(\rho M)}{\partial t} + \frac{\partial(\rho r u M)}{r \partial r} + \frac{\partial(\rho w M)}{\partial z} = 0$$

Where $M = rv + \frac{1}{2}fr^2$

M is the absolute angular momentum; r is the radius from the center of the storm; v is the tangential wind; f is the Coriolis parameter $2\Omega \sin \theta$, where the reference latitude $\theta = 31^\circ\text{N}$ was used; and ρ is the air density retrieved from SAMURAI's output, which used the Dunion moist tropical sounding (Dunion 2011) as its reference state. The radial and vertical winds are denoted by u and w , respectively. Positive values indicate flux convergence of AAM.

A common practice in budget analyses is to further separate each term into an azimuthal mean and perturbation quantity, such that $x = \bar{x} + x'$ where x represents the ρ , u , v , w , and M terms. However, the spatial and temporal resolution of the airborne radar dataset is not sufficient to resolve the perturbation terms. Therefore, the AAM budget analysis was done in the context of the time-average azimuthal mean terms alone, with a focus on fluxes above the boundary layer where friction is negligible. We note that although the sign and magnitude of the eddy terms are unknown they can have a non-negligible effect on the total tendency. The radial and vertical flux divergence calculated in all the legs occur in near-cancellation such that the total tendency field is near-zero

(Fig. 12c,f,i). Without a complete measurement of the eddy fluxes, the total tendency field cannot be completely resolved.

Though the budget cannot be closed, we can gain insight into the ERC process by examining the relative magnitude of the azimuthally-averaged advective terms in the different rainband sectors. The vertical and radial flux divergence and the time tendency of AAM for rainband-C, rainband-S2, and DSE are shown in Fig. 12. In rainband-C, the radial flux convergence of AAM is strongest in the lower levels, with a maximum around 100 km radius and 1 km altitude, and is associated with the inward advection of higher AAM air from the outer radii by the low-level inflow (Fig. 12b). Meanwhile, the strongest vertical flux convergence of AAM is located at 100 km radius and above 4 km altitude, and is associated with the strongest upward vertical velocities observed in this leg (Fig. 7a). Below 4 km altitude, vertical flux divergence of AAM is produced by updrafts that advected lower AAM air upward. The radial flux divergence field is almost completely balanced by the vertical flux divergence field, resulting in weakly positive AAM tendency in rainband-C (Fig. 12c).

Rainband-S2 is associated with a low-level radial flux divergence of AAM by the supergradient outflow, at around 100 km radius and 2 km altitude (Fig. 12e). Above this area of radial flux divergence, a prominent region of radial flux convergence of AAM is seen, and is associated with the inward advection of higher AAM air by the stratiform mid-level inflow (Fig. 8e). Radially inside of the stratiform mid-level inflow, the rising stratiform mid-level outflow produces a flux divergence of AAM at around 100 km radius and 4 km altitude (Fig. 12d). Conversely, rising supergradient outflow beneath this area of flux divergence is associated with a vertical flux convergence of AAM. The radial and vertical flux divergence field combine to produce a weakly negative AAM tendency in rainband-S2 (Fig. 12f)

The momentum budget analysis of DSE is similar in structure to rainband-C, but with generally weaker fluxes. The radial flux of AAM is weakly convergent below 5 km altitude, with near-zero fluxes above (Fig. 12h). Meanwhile, the vertical fluxes of AAM is weakly divergent below 5 km altitude, with similarly near-zero fluxes above (Fig. 12g). Even though DSE is characterized by deeper and slightly stronger inflow (Fig. 9b), the radial fluxes of AAM are weaker in DSE compared to rainband-C. The weaker radial flux of AAM in DSE is because of the weaker radial gradient in AAM compared to the rainband-C. The AAM tendency in DSE is weakly positive (Fig. 12i).

The momentum budget analyses show that the strongest AAM fluxes are associated with the dominantly stratiform sector of Ophelia's rainbands. However, the contribution of either the radial or vertical momentum fluxes to the overall momentum tendency cannot be directly quantified in our analyses. Unresolved eddy fluxes could affect the sign of the AAM tendency, since the AAM tendency is near-zero such that it is weakly positive in rainband-C and DSE (Figs. 12c,i) and weakly negative in rainband-S2 (Fig. 12f). Despite the uncertainties in the total tendency, the individual terms provide insight into the contributions to the tangential wind maximum. While the tangential wind maximum is collocated with the radial flux convergence of AAM in rainband-C (around 100 km radius in Fig. 12b) and DSE (between 60 and 90 km radius in Fig. 12e), the tangential wind maximum in rainband-S2 is associated with the radial flux convergence above 3 km and vertical flux convergence below 3 km (around 100 km radius in Fig. 12d).

We hypothesize that the elevated tangential wind maximum associated with the radial convergence of AAM in the stratiform mid-level inflow contributes to the peak tangential wind below via the development of the supergradient forcing and subsequent vertical flux convergence of AAM from the boundary layer. In other words, some local maximum in the tangential winds has to be present first in order for the supergradient winds to occur. The supergradient outflow is in response

to the tangential wind maximum produced from enhanced AAM convergence by the descending mid-level inflow in the region. The positive vertical flux convergence of AAM in rainband-S2 (Fig. 12d) associated with the supergradient outflow then acts to sustain and lower the tangential wind maximum. We discuss this mechanism in more detail in the following section.

5. Axisymmetric View and Secondary Eyewall Formation Mechanism

The discussions thus far have focused on the mean kinematics of the different rainband sectors. To determine their relative impact on the overall storm structure, azimuthal averages of vertical, radial, and tangential winds were plotted alongside azimuthally-averaged radar reflectivity (Fig. 13) to provide an axisymmetric view of the rainband dynamics. A portion of rainband-S1 was used to fill in the gap between the downwind end of rainband-C and the upwind end of rainband-S2. As shown in Fig. 13, the axisymmetric kinematics resemble a combination of both convective and stratiform kinematics. A shallow inflow layer can be seen below approximately 2 km altitude throughout the whole radial region of Ophelia's rainbands (Fig. 13b). Simultaneously, a descending mid-level inflow can also be observed, originating from 7 km altitude at 160 km radius to 3 km altitude at 90 km radius, with a tangential wind maximum observed at 2 km altitude and 100 km radius (Fig. 13c). This axisymmetric tangential wind maximum resembles that seen in rainband-S2, indicating that dominantly stratiform kinematics strongly project onto the axisymmetric tangential winds. Finally, a rising outflow is found beginning around 4 km altitude at 90 km radius (Fig. 13a,b). Similarly, axisymmetric radial AAM flux convergence can be seen in the lower levels, followed by a second region of radial flux convergence in the mid-levels (Fig. 14b). A similar but opposite sign is observed in the axisymmetric vertical AAM flux divergence field (Fig. 14a), producing a near-zero AAM tendency (Fig. 14c).

An additional analysis was done using observations from a second NOAA P-3 aircraft (hereafter N42). The N42 aircraft flew multiple radial passes at around 850 to 880 mb level from 1808 UTC on 11 September through 0008 UTC on 12 September, as the NRL and N43 aircraft were sampling the rainbands. N42 deployed 17 dropsondes within 150 km of the storm center. Dropsondes transmit humidity, pressure, and temperature data as it descends through the atmosphere, providing their respective vertical profiles from the deployment altitude to the surface. Horizontal winds can also be retrieved from the transmitted GPS information. Flight-level and dropsonde data from the N42 observation were analyzed using an axisymmetric version of SAMURAI with 1 km grid spacing. Due to uneven sampling and noise in the flight level and dropsonde data, the data was smoothed in the radial direction with a low-pass Gaussian filter to remove spatial scales less than 20 km. The derived radial pressure gradient was then averaged in the vertical to produce a representative gradient for an approximate slab boundary layer between the surface and 1.4 km. However, the vertical averaging precludes a height-resolved analysis. The analysis then provides the axisymmetric mass and wind fields that allow for the calculation of the low-level agradient force, similar to calculations made in Bell and Montgomery (2008) and Bell et al. (2012b) but with an improved methodology. The agradient force per unit mass (AF) can then be calculated as:

$$AF = -\frac{1}{\rho} \frac{\delta p}{\delta r} + \frac{v^2}{r} + fv \quad (1)$$

The first term on the right-hand side of the equation is the radial pressure gradient force (PGF), the second term is the centrifugal force, and the third term is the Coriolis force. The individual forces, their sum, and the tangential velocity were calculated from the in situ analysis at 1.2 km altitude and shown in Fig. 15. For simplicity, the centrifugal and Coriolis forces were added and plotted as a “gradient wind force,” with the PGF plotted separately. In addition, the axisymmetric tangential velocity and corresponding gradient wind force from the independently calculated radar

analysis were also calculated and interpolated to 1.2 km altitude for comparison (dashed lines in Fig. 15).

The gradient wind force peaks at around 40 km radius and gradually decreases at larger radii (blue line, Fig. 15). Meanwhile, the PGF is characterized by two minima, one located at 40 km radius and the other at 120 km, with a maximum at 85 km radius (green line). The AF is largely determined by the PGF, with positive AF values between 60 and 110 km radius (yellow line). This positive AF region corresponds to the occurrence of supergradient winds at 1.2 km, in response to the axisymmetric tangential wind maximum located in its vicinity around 100 km radius.

Synthesizing the results, we hypothesize Ophelia’s secondary eyewall formation occurred in the following manner. Ophelia was located over cold SSTs for an extended period of time, which resulted in a weakening primary wind maximum and reduced convective vigor that allowed stratiform rainband kinematics to dominate. The mid-level inflow of Ophelia’s dominantly stratiform rainbands efficiently converged angular momentum above the boundary layer, spinning up a secondary tangential wind maximum in the mid- to low-levels that strongly contributed to the azimuthal mean tangential wind field. The secondary tangential wind maximum contributed to increased low-level supergradient winds and corresponding outflow, which converged with the subgradient low-level inflow to form a secondary eyewall. However, due to limitations in the radar observations, we cannot exclude the existence of boundary layer agradient forcing prior to the observation of the supergradient winds observed here.

While the results presented above showed different rainband kinematics between rainband-C, rainband-S2, and DSE, we also note that the rainbands were sampled in succession such that rainband-C was sampled first, followed by rainband-S2 and DSE. Therefore, we hypothesize that the convergence between the low-level supergradient outflow and the storm-scale low-level inflow had already occurred in the DSE in Ophelia’s ERC, producing dominantly convective kinematics

associated with a secondary eyewall there. The stratiform-to-convective transition downwind of a dominantly stratiform rainband is consistent with analyses of Hurricane Earl (2010) by Didlake et al. (2018) and Hurricane Irma (2017) by Fischer et al. (2020), suggesting this transition may be common to different ERC events despite the different environmental conditions in Ophelia.

Ophelia's ERC was therefore ‘unconventional’ with respect to its weaker intensity and cold SSTs, and also differs somewhat from a canonical ERC in that the primary eyewall was already weakening before the secondary eyewall was completely developed. However, the physical mechanisms by which the ERC occurred appear to be similar in several ways to those documented in other storms.

6. Conclusion

Hurricane Ophelia (2005) underwent an unconventional eyewall replacement cycle (ERC) that occurred while Ophelia was a weak Category 1 hurricane located over cold sea surface temperatures ($\sim 23^{\circ}\text{C}$). Using the flight-level dataset from USAF aircraft hurricane reconnaissance missions into Ophelia, the flight-level tangential wind field was shown to evolve similarly to a storm undergoing a conventional ERC, with the corresponding satellite microwave imagery showing a similar evolution in convective activity. However, concentric rings of deep convective eyewalls typical of a canonical ERC was not observed. Instead, the secondary eyewall was only partially apparent in the 37-GHz imagery, associated with mostly low-level warm rain.

The weakening phase of Ophelia's ERC, during which a secondary wind maximum typically intensifies, was observed on 11 September 2005 as part of the Hurricane Rainband and Intensity Change Experiment (RAINEX). Airborne radar data were obtained from the Naval Research Laboratory (NRL) and the National Oceanic and Atmospheric Administration (NOAA) P-3 aircraft

that flew simultaneously along a rainband, allowing for quad-Doppler wind retrievals of rainband kinematics using a variational wind synthesis technique.

The distant rainbands of Hurricane Ophelia were characterized by dominantly convective precipitation, with low-level inflow and upper-level outflow. A relatively weak and localized tangential wind maximum was found in the lower levels of the rainband inner region, likely associated with convective scale processes. Downwind and closer to the inner core, the dominantly stratiform sector of Ophelia’s rainbands was characterized by mid-level inflow, with outflow above and below. Out of all the rainband sectors analyzed, the strongest tangential wind maximum can be found radially inward of the mid-level inflow. Observations of both convective and stratiform rainband kinematics corroborated observations made in previous studies (Hence and Houze 2008; Didlake and Houze 2009, 2013b). Downwind of the dominantly stratiform rainbands, rainband kinematics gradually transitioned into being dominantly convective, with a deep-layer low-level inflow and upper-level outflow. We hypothesize that this dominantly convective portion of the rainband was the developing secondary eyewall, although enhanced tangential winds and reflectivity in the stratiform portion of the rainbands also showed characteristics of secondary eyewall development. Due to temporal and spatial sampling limitations we were unable to observe the subsequent detailed evolution of the developing secondary eyewall, but the results described herein suggest both the stratiform and convective portions of the rainband played a role in different stages of the ERC process.

Momentum budget analyses showed that the strongest fluxes of absolute angular momentum (AAM) were associated with the dominantly stratiform rainband, where the strongest tangential winds were also found. However, a direct relationship between either the radial or vertical fluxes of AAM and the time tendency of the tangential winds cannot be determined due to (i) the near-cancellation of the radial flux of AAM with the vertical flux of AAM, and (ii) the unresolved

eddy fluxes in the momentum budget. Nonetheless, the analysis suggests that the strong radial AAM flux associated with the stratiform mid-level inflow was responsible for spinning up the tangential wind maximum in the dominantly stratiform rainbands. This mid-level tangential wind maximum projects strongly onto the axisymmetric tangential winds, indicating that the stratiform mid-level inflow had a substantial influence on the azimuthal mean structure. An axisymmetric analysis of the flight-level and dropsonde data deployed from a second NOAA P-3 aircraft during the same intensive observing period indicate the presence of supergradient winds in the low-levels associated with this tangential wind maximum.

Therefore, we hypothesize that Ophelia's ERC occurred in the following manner:

1. Ophelia was located over colder sea surface temperatures for an extended period of time, which is believed to have led to the weakening of the inner eyewall. The contribution of the colder sea surface temperatures to the fraction of observed stratiform and deep convection in the rainbands is unclear, but we would expect reduced convective vigor due to reduced surface fluxes during this period.
2. The dominantly stratiform rainbands efficiently converged AAM above the boundary layer and spun up a mid-level tangential wind maximum. The tangential wind maximum is the strongest out of all the rainband sectors analyzed and strongly projected onto the axisymmetric tangential wind field.
3. The axisymmetric tangential wind maximum produced supergradient forcing in the low-levels, which enhanced the convergence in and near the top of the boundary layer that led to the development of the secondary eyewall.

We believe the process summarized above had already taken place in what we hypothesize to be the developing secondary eyewall sector of Ophelia’s rainbands, but had yet to take place in the dominantly convective and dominantly stratiform rainbands at the time of the radar observations.

Our analysis is consistent with the findings of previous studies on the role of unbalanced boundary layer dynamics in secondary eyewall formation (Huang et al. 2012; Fischer et al. 2020). Our hypothesis does not dismiss the role of deep convection in Ophelia’s ERC, since convection was re-invigorated as the storm moved over warmer SSTs in the the storm’s re-intensification phase. The observations suggest that dominantly stratiform rainbands were not the sole mechanism through which the broadening of the tangential wind field in a conventional ERC could occur, but rather that they may have played a more significant role in this particular scenario due to the weaker storm intensity and colder SSTs.

The exact sequence of events, including the typical location in which secondary eyewall formation first occur, warrants further investigation. Additional observations of ERCs in a variety of different environments and stages of the TC life-cycle are needed to better understand the processes involved. Additional investigation is also required on how well these observed rainband kinematics and their impacts on TC structure and intensity are represented in numerical weather prediction models to improve intensity forecasts in the future.

Data Availability Statement. Data analyzed in this study were a re-analysis of existing data, which are openly available and documented at locations cited in the reference section. Data specific to the RAINEX field campaign can be found at https://data.eol.ucar.edu/master_lists/generated/rainex/. Processed observational data used in this study is available upon request.

Acknowledgments. This research was supported by the National Science Foundation awards AGS-1701225 and OAC-1661663 and Office of Naval Research Award N000142012069. Naufal Razin was also supported by the NASA Earth and Space Science Fellowship award 80NSSC18K1349. We would like to acknowledge the RAINEX and IFEX science teams including the NCAR, the Naval Research Lab, NOAA Aircraft Operations Center, and NOAA Hurricane Research Division of AOML for their data collection and archiving efforts. We would also like to thank Eleanor Casas for her feedback on the manuscript prior to submission, and Michael Fischer, Anthony Didlake and an anonymous reviewer for their insightful comments.

References

- Banzon, V., T. M. Smith, T. M. Chin, C. Liu, and W. Hankins, 2016: A long-term record of blended satellite and in situ sea-surface temperature for climate monitoring, modeling and environmental studies. *Earth Syst. Sci. Data*, **8**, 165–176, doi:10.5194/essd-8-165-2016.
- Barnes, G. M., E. J. Zipser, D. Jorgensen, and F. Marks, Jr., 1983: Mesoscale and convective structure of a hurricane rainband. *J. Atmos. Sci.*, **40**, 2125–2137, doi:10.1175/1520-0469(1983)040<2125:MACSOA>2.0.CO;2.
- Bell, M. M., M. Dixon, W.-C. Lee, B. Javornik, J. C. DeHart, and T.-Y. Cha, 2020: nsf-lrose/lrose-cyclone: lrose-cyclone-20200110. NSF-LROSE, doi: 10.5281/zenodo.3604387.
- Bell, M. M., W.-C. Lee, C. A. Wolff, and H. Cai, 2013: A Solo-based automated quality control algorithm for airborne tail Doppler radar data. *J. Appl. Meteor. Climatol.*, **52**, 2509–2528, doi: 10.1175/JAMC-D-12-0283.1.
- Bell, M. M., and M. T. Montgomery, 2008: Observed structure, evolution, and potential intensity of Category 5 Hurricane Isabel (2003) from 12 to 14 September. *Mon. Wea. Rev.*, **136**, 2023–

2046, doi:10.1175/2007MWR1858.1.

Bell, M. M., M. T. Montgomery, and K. A. Emanuel, 2012a: Air-sea enthalpy and momentum exchange at major hurricane wind speeds observed during CBLAST. *J. Atmos. Sci.*, **69**, 3197–3222, doi:10.1175/JAS-D-11-0276.1.

Bell, M. M., M. T. Montgomery, and W.-C. Lee, 2012b: An axisymmetric view of concentric eyewall evolution in Hurricane Rita (2005). *J. Atmos. Sci.*, **69**, 2414–2432, doi:10.1175/JAS-D-11-0167.1.

Beven, J., and H. D. Cobb, III, 2006: Tropical cyclone report: Hurricane Ophelia. National Hurricane Center.

Dare, R. A., and J. L. McBride, 2011: The threshold sea surface temperature condition for tropical cyclogenesis. *J. Climate*, **24**, 4570–4576, doi:10.1175/JCLI-D-10-05006.1.

DeMaria, M., M. Mainelli, L. K. Shay, J. A. Knaff, and J. Kaplan, 2005: Further improvements to the statistical hurricane intensity prediction scheme SHIPS. *Wea. Forecasting*, **20**, 531–543, doi:10.1175/WAF862.1.

DeMaria, M., C. R. Sampson, J. A. Knaff, and K. D. Musgrave, 2014: Is tropical cyclone intensity guidance improving? *Bull. Amer. Meteor. Soc.*, **95**, 387–398, doi:10.1175/BAMS-D-12-00240.1.

Didlake, A. C., Jr., and R. A. Houze, Jr., 2009: Convective-scale downdrafts in the principal rainband of Hurricane Katrina (2005). *Mon. Wea. Rev.*, **137**, 3269–3293, doi:10.1175/2009MWR2827.1.

Didlake, A. C., Jr., and R. A. Houze, Jr., 2013a: Convective-scale variations in the inner-core rainbands of a tropical cyclone. *J. Atmos. Sci.*, **70**, 504–523, doi:10.1175/JAS-D-12-0134.1.

- Didlake, A. C., Jr., and R. A. Houze, Jr., 2013b: Dynamics of the stratiform sector of a tropical cyclone rainband. *J. Atmos. Sci.*, **70**, 1891–1911, doi:10.1175/JAS-D-12-0245.1.
- Didlake, A. C., Jr., P. Reasor, R. Rogers, and W. Lee, 2018: Dynamics of the transition from spiral rainbands to a secondary eyewall in Hurricane Earl (2010). *J. Atmos. Sci.*, **75**, 2909–2929, doi:10.1175/JAS-D-17-0348.1.
- Dougherty, E. M., J. Molinari, R. F. Rogers, J. A. Zhang, and J. P. Kossin, 2018: Hurricane Bonnie (1998): Maintaining intensity during high vertical wind shear and an eyewall replacement cycle. *Mon. Wea. Rev.*, **146**, 3383–3399, doi:10.1175/MWR-D-18-0030.1.
- Dunion, J. P., 2011: Rewriting the climatology of the Tropical North Atlantic and Caribbean Sea atmosphere. *J. Climate*, **24**, 893–908, doi:10.1175/2010JCLI3496.1.
- Fischer, M. S., R. F. Rogers, and P. D. Reasor, 2020: The rapid intensification and eyewall replacement cycles of Hurricane Irma (2017). *Mon. Wea. Rev.*, **148**, 981–1004, doi:10.1175/MWR-D-19-0185.1.
- Foerster, A. M., M. M. Bell, P. A. Harr, and S. C. Jones, 2014: Observations of the eyewall structure of Typhoon Sinlaku (2008) during the transformation stage of extratropical transition. *Mon. Wea. Rev.*, **142**, 3372–3392, doi:doi.org/10.1175/MWR-D-13-00313.1.
- Fudeyasu, H., and Y. Wang, 2011: Balanced contribution to the intensification of a tropical cyclone simulated in TCM4: outer-core spinup process. *J. Atmos. Sci.*, **68**, 430–449, doi:10.1175/2010JAS3523.1.
- Guimond, S. R., J. A. Zhang, J. W. Sapp, and S. J. Frasier, 2018: Coherent turbulence in the boundary layer of Hurricane Rita (2005) during an eyewall replacement cycle. *J. Atmos. Sci.*, **75**, 3071–3093, doi:10.1175/JAS-D-17-0347.1.

Hence, D. A., and R. A. Houze, Jr., 2008: Kinematic structure of convective-scale elements in the rainbands of Hurricanes Katrina and Rita (2005). *J. Geophys. Res.*, **113**, D15 108, doi:10.1029/2007JD009429.

Hence, D. A., and R. A. Houze, Jr., 2012: Vertical structure of tropical cyclone rainbands as seen by the TRMM precipitation radar. *J. Atmos. Sci.*, **69**, 2644–2661, doi:10.1175/JAS-D-11-0323.1.

Hildebrand, P. H., and Coauthors, 1996: The ELDORA/ASTRAIA airborne Doppler weather radar: high-resolution observations from TOGA COARE. *Bull. Amer. Meteor. Soc.*, **77**, 213–232, doi:10.1175/1520-0477(1996)077<0213:TEADWR>2.0.CO;2.

Houze, R. A., Jr., 2010: Review: clouds in tropical cyclones. *Mon. Wea. Rev.*, **138**, 293–344, doi:10.1175/2009MWR2989.1.

Houze, R. A., Jr., S. S. Chen, B. F. Smull, W.-C. Lee, and M. M. Bell, 2007: Hurricane intensity and eyewall experiment. *Science*, **315**, 1235–1239.

Houze, R. A., Jr., and Coauthors, 2006: The hurricane rainband and intensity change experiment: observations and modeling of Hurricanes Katrina, Ophelia, and Rita. *Bull. Amer. Meteor. Soc.*, **87**, 1503–1521, doi:10.1175/BAMS-87-11-1503.

Huang, Y.-H., M. T. Montgomery, and C.-C. Wu, 2012: Concentric eyewall formation in Typhoon Sinlaku (2008). part II: Axisymmetric dynamical processes. *J. Atmos. Sci.*, **69**, 662–674, doi:10.1175/JAS-D-11-0114.1.

Jarvinen, B. R., C. J. Neumann, and M. A. S. Davis, 1984: A tropical cyclone data tape for the North Atlantic basin, 1886–1983: contents, limitations, and uses. NOAA Tech. Memo. NWS/NHC 22, NOAA/National Hurricane Center, Miami, FL, 21 pp.

Jorgensen, D. P., T. Matejka, and J. D. DuGranrut, 1996: Multi-beam techniques for deriving wind fields from airborne Doppler radars. *Meteor. Atmos. Phys.*, **59**, 83–104, doi: 10.1007/BF01032002.

Knapp, K. R., and S. L. Wilkins, 2018: Gridded satellite (GridSat) GOES and CONUS data. *Earth Syst. Sci. Data*, **10**, 1417–1425, doi:10.5194/essd-10-1417-2018.

Kossin, P., J., and M. Sitkowski, 2009: An objective model for identifying secondary eyewall formation in hurricanes. *Mon. Wea. Rev.*, **137**, 876–892, doi:10.1175/2008MWR2701.1.

Landsea, C. W., and J. L. Franklin, 2013: Atlantic hurricane database uncertainty and presentation of a new database format. *Mon. Wea. Rev.*, **141**, 3576–3592, doi:10.1175/MWR-D-12-00254.1.

McAdie, C. J., C. W. Landsea, C. J. Neumann, J. E. David, E. S. Blake, and G. R. Hammer, 2009: *Tropical cyclones of the North Atlantic Ocean, 1951–2006 (6th Ed.)*. Historical Climatology Series, No. 6-2, National Climatic Data Center, 238 pp.

Montgomery, M. T., and R. J. Kallenbach, 1997: A theory for vortex Rossby-waves and its application to spiral bands and intensity changes in hurricanes. *Quart. J. Roy. Meteor. Soc.*, **123**, 435–465, doi:10.1002/qj.49712353810.

Moon, Y., and D. S. Nolan, 2010: The dynamic response of the hurricane wind field to spiral rainband heating. *J. Atmos. Sci.*, **67**, 1779–1805, doi:10.1175/2010JAS3171.1.

NRL, 2005: NRL Tropical Cyclone Page: Hurricane Ophelia (2005). Accessed 3 November 2016, <https://www.nrlmry.navy.mil/TC.html>.

Razin, M. N., 2018: The unconventional eyewall replacement cycle of Hurricane Ophelia (2005). M.S. thesis, Department of Atmospheric Science, Colorado State University, 57 pp.

Samsury, C. E., and E. J. Zipser, 1995: Secondary wind maxima in hurricanes: airflow and relationship to rainbands. *Mon. Wea. Rev.*, **123**, 3502–3517, doi:10.1175/1520-0493(1995)123<3502:SWMIHA>2.0.CO;2.

Sitkowski, M., J. P. Kossin, and C. M. Rozoff, 2011: Intensity and structure changes during hurricane eyewall replacement cycles. *Mon. Wea. Rev.*, **139**, 3829–3847, doi:10.1175/MWR-D-11-00034.1.

Smith, A. W., 2016: The role of air-sea interaction in structure and intensity change in Hurricane Ophelia (2005): coupled modeling and RAINEX observations. M.S. thesis, Rosenstiel School of Marine and Atmospheric Science (RSMAS), University of Miami, 142 pp.

Smith, R. K., M. T. Montgomery, and V. S. Nguyen, 2009: Tropical cyclone spin-up revisited. *Quart. J. Roy. Meteor. Soc.*, **135**, 1321–1335, doi:10.1002/qj.428.

Testud, J., P. H. Hildebrand, and W.-C. Lee, 1995: A procedure to correct airborne Doppler radar data for navigation errors using the echo returned from the earth's surface. *J. Atmos. Oceanic Technol.*, **12**, 800–820, doi:10.1175/1520-0426(1995)012<0800:APTCAD>2.0.CO;2.

Vigh, J. L., 2015: VDM+: The Enhanced Vortex Data Message Dataset (Version 1.100). Tropical Cyclone Data Project, National Center for Atmospheric Research, Research Applications Laboratory, Boulder, Colorado., [Available online at: <http://dx.doi.org/10.5065/D61Z42GH>.] Accessed 21 February 2017.

Vigh, J. L., and Coauthors, 2016: FLIGHT+: The Extended Flight Level Dataset for Tropical Cyclones (Version 1.1). Tropical Cyclone Data Project, National Center for Atmospheric Research, Research Applications Laboratory, Boulder, Colorado., [Available online at: <http://dx.doi.org/10.5065/D6WS8R93>.] Accessed 30 November 2016.

Willoughby, H. E., F. D. Marks, Jr., and R. J. Feinberg, 1984: Stationary and moving convective bands in hurricanes. *J. Atmos. Sci.*, **41**, 3189–3211, doi:10.1175/1520-0469(1984)041<3189: SAMCBI>2.0.CO;2.

Wunsch, K. E. D., and A. C. Didlake, Jr., 2018: Analyzing tropical cyclone structures during secondary eyewall formation using aircraft in situ observations. *Mon. Wea. Rev.*, **146**, 3977–3993, doi:10.1175/MWR-D-18-0197.1.

LIST OF TABLES

Table 1. The start and end of observation periods for the NRL and N43 aircraft on September 11th 2005, and their corresponding label and rainband type for discussion purposes.

41

TABLE 1. The start and end of observation periods for the NRL and N43 aircraft on September 11th 2005, and their corresponding label and rainband type for discussion purposes.

Aircraft	Start Time (UTC)	End Time (UTC)	Label	Rainband Type
NRL	185301	190858	rainband-C	Dominantly
N43	185400	191037		convective
NRL	201801	210558	rainband-S1	Dominantly
N43	203002	210557		stratiform
NRL	213341	215158	rainband-S2	Dominantly
N43	212003	214257		stratiform
NRL	215401	221059	DSE	Developing
N43	215403	220315		secondary eyewall

LIST OF FIGURES

- Fig. 1.** (a) Radar reflectivity at 2 km altitude of the four rainband sectors where quad-Doppler observations are available (rainband-C, rainband-S1, rainband-S2, and DSE) from the RAINEX observation period on September 11th 2005, overlaid on a gridded satellite visible image of Ophelia at 2100 UTC with longitude and latitude on the respective x- and y-axis. The NRL and N43 flight tracks are indicated by the solid and dotted lines, respectively. A large portion of rainband-S2 is rainband-S1 sampled at a later period and are overlaid accordingly. Detailed observation times for both aircraft can be found in Table 1. Location of individual cross-sections (CS-C - CS-DSE) are indicated with dashed lines. (b) The result of the convective-stratiform partitioning (Didlake and Houze 2009) on the radar reflectivity field for each of the rainband sectors, plotted with the x- and y- distances relative to the analysis center on the respective x- and y- axis. The black lines serve to orientate the reader on the geometry and extent of the sector averaging for rainband-C (solid), rainband-S2 (dashed), and DSE (dotted). The shear direction and magnitude close to the observation time is represented by the arrow in the top-right corner of each figure. 44
- Fig. 2.** Ophelia's track and intensity from the National Hurricane Center's best-track dataset. The intensity classifications are tropical depression (TD; turquoise), tropical storm (TS; green), and Category 1 Hurricane (Cat 1; yellow). A select few best-track center locations and the corresponding dates and times in UTC are labeled along the storm track. 45
- Fig. 3.** The evolution of Ophelia's intensity, defined by the maximum 1-minute sustained wind at 10 meters (solid line, knots) and minimum sea-level pressure (dotted line, hPa) from the National Hurricane Center's best-track dataset. The hatched line indicates the approximate time when quad-Doppler observations were made on September 11th. The colored lines mark the approximate time of the USAF hurricane reconnaissance missions for corresponding observed tangential wind profile in Fig. 5. 46
- Fig. 4.** Daily average sea surface temperature (SST; °C) overlaid with Ophelia's track up until 1800 UTC on the corresponding day. The dates are labeled in the top right corner of each figure. 47
- Fig. 5.** The evolution of Ophelia's azimuthal-mean flight-level (700 hPa) tangential wind profile as observed from nine US Air Force aircraft reconnaissance missions. The start time of the first radial pass during each reconnaissance mission is labeled and also indicated in the same color on Ophelia's intensity plot (Fig. 3). 48
- Fig. 6.** Satellite microwave brightness temperatures in the ice-scattering channels (horizontally-polarized 85 - 91 GHz) of Hurricane Ophelia as it underwent an eyewall replacement cycle, courtesy of the Naval Research Laboratory. 49
- Fig. 7.** Sector average (a) vertical, (b) radial and (c) tangential velocities (m s^{-1}) with overlaid contours of sector average reflectivity (dBZ), and (d) the sector average reflectivity (dBZ) with overlaid wind vectors in rainband-C. The 30-dBZ contour is highlighted in (a), (b), and (c) to help distinguish the reflectivity columns (see text). 50
- Fig. 8.** Sector average (a) vertical, (b) radial and (c) tangential velocities (m s^{-1}) with overlaid contours of sector average reflectivity (dBZ), and (d) the sector average reflectivity (dBZ) with overlaid wind vectors in rainband-S2. 51
- Fig. 9.** Sector average (a) vertical, (b) radial and (c) tangential velocities (m s^{-1}) with overlaid contours of sector average reflectivity (dBZ), and (d) the sector average reflectivity (dBZ) with overlaid wind vectors in the developing secondary eyewall (DSE). 52

- Fig. 10.** Individual cross-sections of tangential velocity (left column; m s^{-1}) and radial velocity (right column; m s^{-1}) in each of the rainband sectors where quad-Doppler observations are available. Overlaid are contours of reflectivity (dBZ). The location of the cross-sections (CS) correspond to the lines labeled in Fig. 1a 53
- Fig. 11.** (a) 85-GHz microwave brightness temperatures of Hurricane Ophelia at the start of the research flights, and (b) 37-GHz and (c) 85-GHz microwave brightness temperatures of Hurricane Ophelia after the conclusion of the research flights on the 11th of September. 54
- Fig. 12.** Vertical flux of absolute angular momentum (left column), radial flux of absolute angular momentum (middle column), and absolute angular momentum tendency (right column) calculated from rainband-C (top), rainband-S2 (middle), and DSE (bottom). Overlaid are contours of sector absolute angular momentum ($\times 10^6 \text{ m}^2 \text{ s}^{-1}$; solid black) and contours of 30, 35, and 40 m s^{-1} tangential winds (dashed magenta). 55
- Fig. 13.** Axisymmetric (a) vertical, (b) radial and (c) tangential velocities (m s^{-1}) with overlaid contours of axisymmetric reflectivity (dBZ), and (d) the axisymmetric reflectivity (dBZ) with overlaid wind vectors. 56
- Fig. 14.** Axisymmetric vertical flux of absolute angular momentum (left column), radial flux of absolute angular momentum (middle column), and absolute angular momentum tendency (right column). Overlaid are contours of axisymmetric absolute angular momentum ($\times 10^6 \text{ m}^2 \text{ s}^{-1}$; solid black) and contours of 30, 35, and 40 m s^{-1} tangential winds (dashed magenta). 57
- Fig. 15.** Radial profiles of agradient force (yellow line) and its components: (i) pressure gradient force (green line) and (ii) the sum of the centrifugal and Coriolis forces as a “gradient wind force” (blue line). Also included is the axisymmetric tangential winds (black line). All fields are plotted at 1.2 km altitude, with the solid lines denoting fields computed from the axisymmetric SAMURAI analysis using in-situ data, and dotted lines denoting fields computed using the axisymmetric tangential winds from the SAMURAI radar analysis. 58

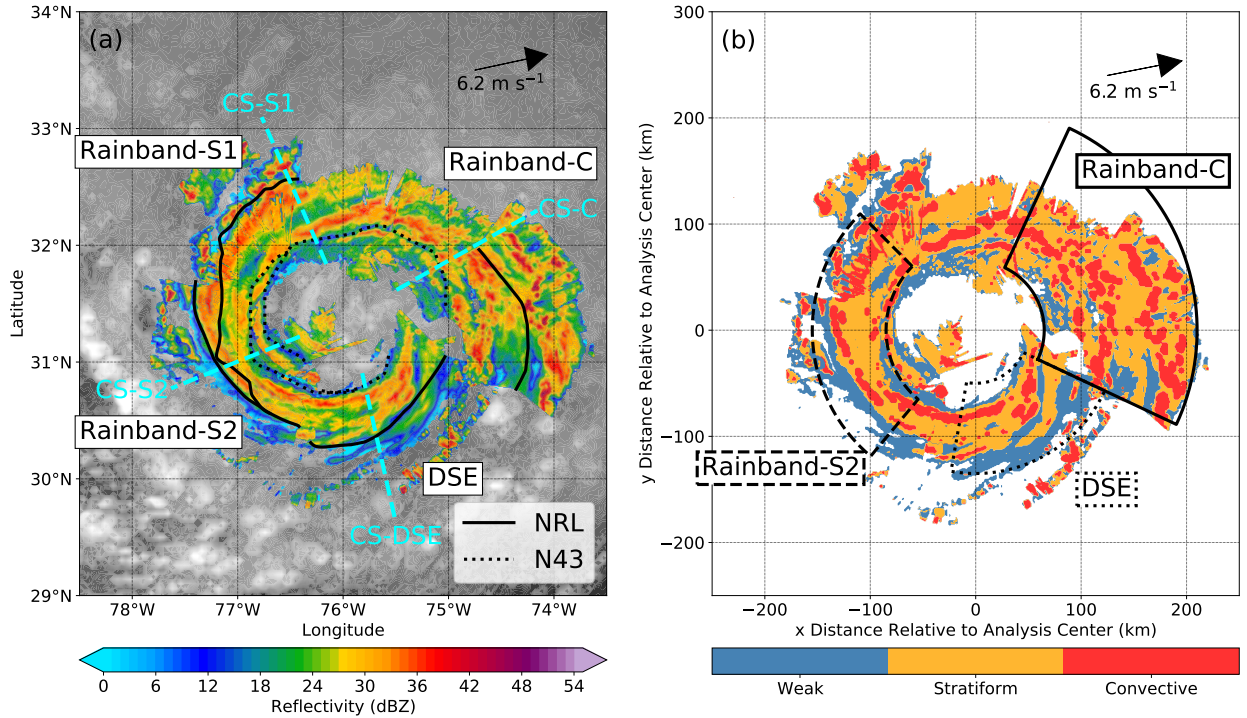


FIG. 1. (a) Radar reflectivity at 2 km altitude of the four rainband sectors where quad-Doppler observations are available (rainband-C, rainband-S1, rainband-S2, and DSE) from the RAINEX observation period on September 11th 2005, overlaid on a gridded satellite visible image of Ophelia at 2100 UTC with longitude and latitude on the respective x- and y-axis. The NRL and N43 flight tracks are indicated by the solid and dotted lines, respectively. A large portion of rainband-S2 is rainband-S1 sampled at a later period and are overlaid accordingly. Detailed observation times for both aircraft can be found in Table 1. Location of individual cross-sections (CS-C - CS-DSE) are indicated with dashed lines. (b) The result of the convective-stratiform partitioning (Didlake and Houze 2009) on the radar reflectivity field for each of the rainband sectors, plotted with the x- and y- distances relative to the analysis center on the respective x- and y- axis. The black lines serve to orientate the reader on the geometry and extent of the sector averaging for rainband-C (solid), rainband-S2 (dashed), and DSE (dotted). The shear direction and magnitude close to the observation time is represented by the arrow in the top-right corner of each figure.

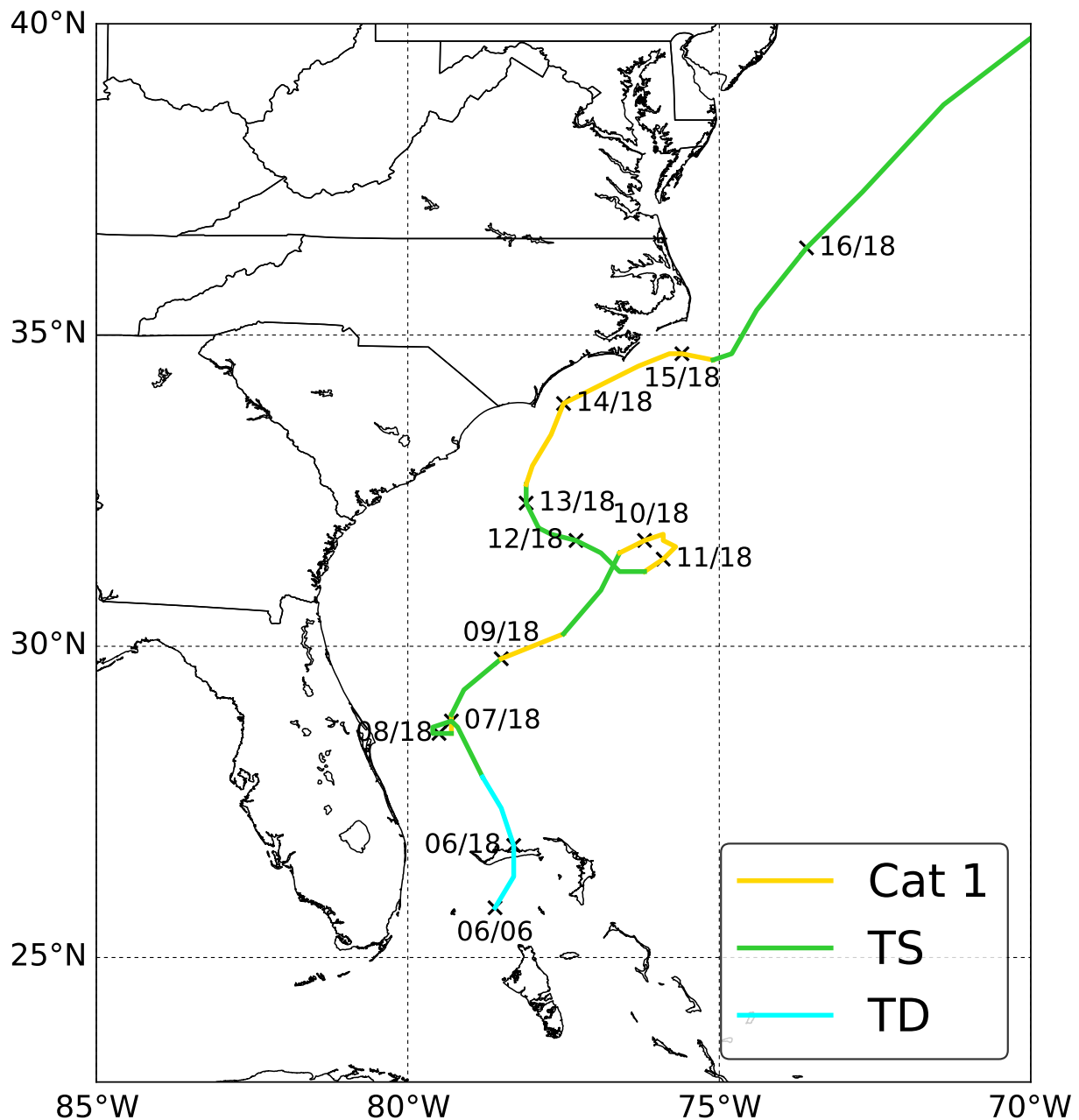


FIG. 2. Ophelia's track and intensity from the National Hurricane Center's best-track dataset. The intensity classifications are tropical depression (TD; turquoise), tropical storm (TS; green), and Category 1 Hurricane (Cat 1; yellow). A select few best-track center locations and the corresponding dates and times in UTC are labeled along the storm track.

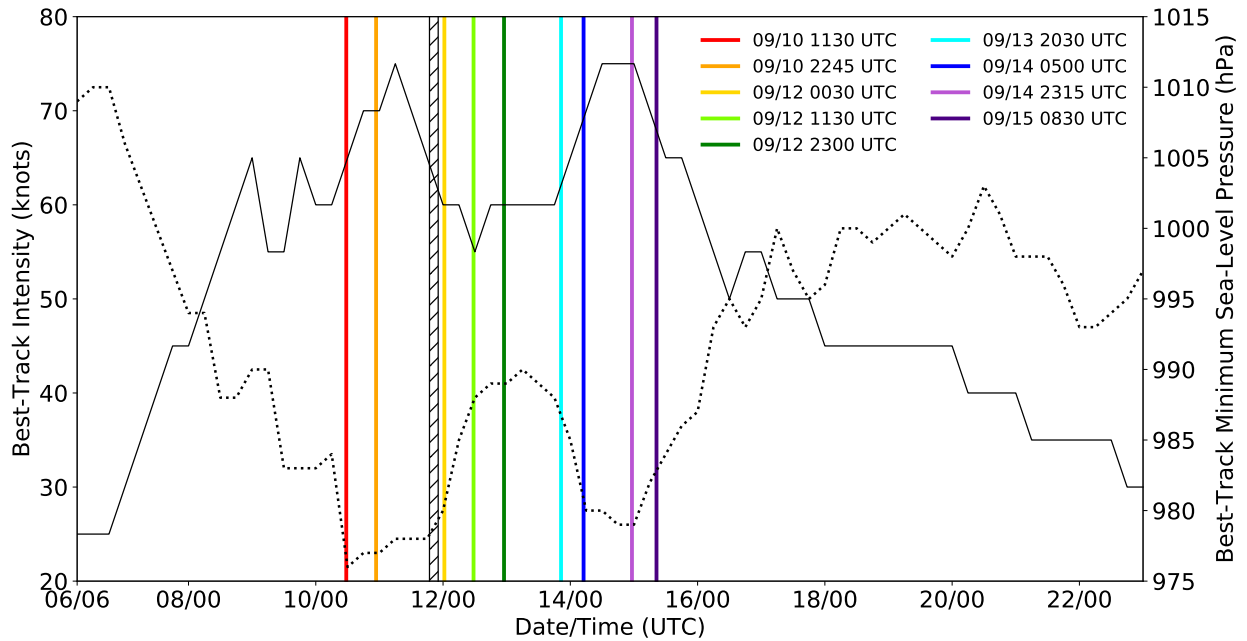


FIG. 3. The evolution of Ophelia's intensity, defined by the maximum 1-minute sustained wind at 10 meters (solid line, knots) and minimum sea-level pressure (dotted line, hPa) from the National Hurricane Center's best-track dataset. The hatched line indicates the approximate time when quad-Doppler observations were made on September 11th. The colored lines mark the approximate time of the USAF hurricane reconnaissance missions for corresponding observed tangential wind profile in Fig. 5.

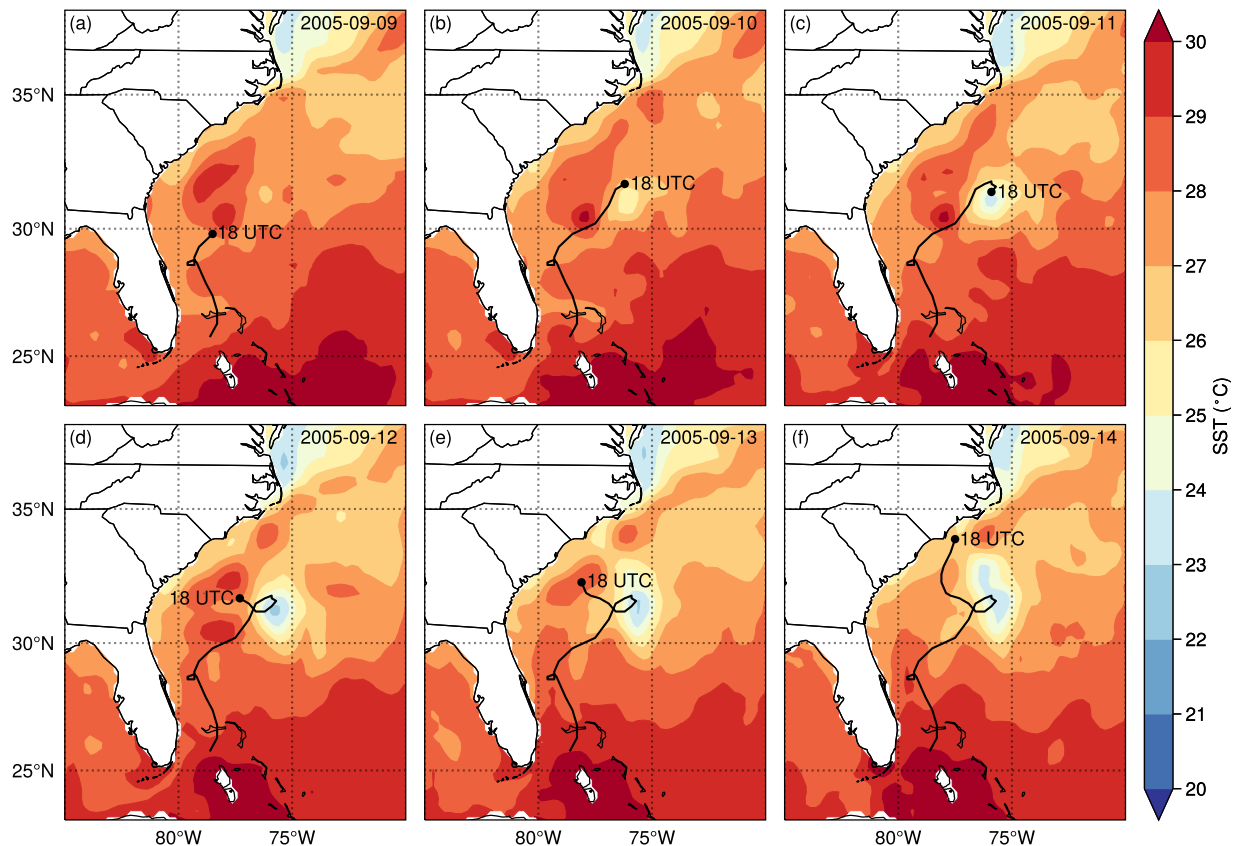


FIG. 4. Daily average sea surface temperature (SST; °C) overlaid with Ophelia's track up until 1800 UTC on the corresponding day. The dates are labeled in the top right corner of each figure.

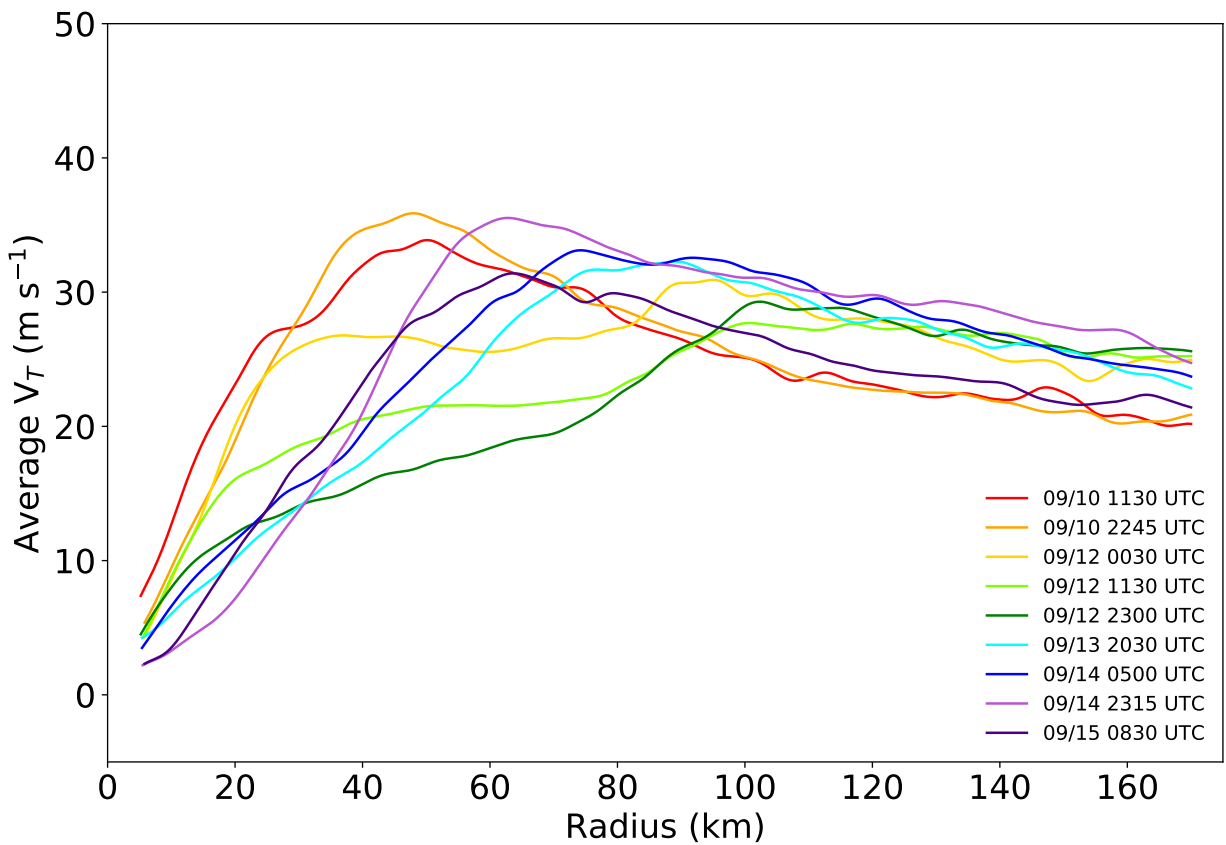


FIG. 5. The evolution of Ophelia's azimuthal-mean flight-level (700 hPa) tangential wind profile as observed from nine US Air Force aircraft reconnaissance missions. The start time of the first radial pass during each reconnaissance mission is labeled and also indicated in the same color on Ophelia's intensity plot (Fig. 3).

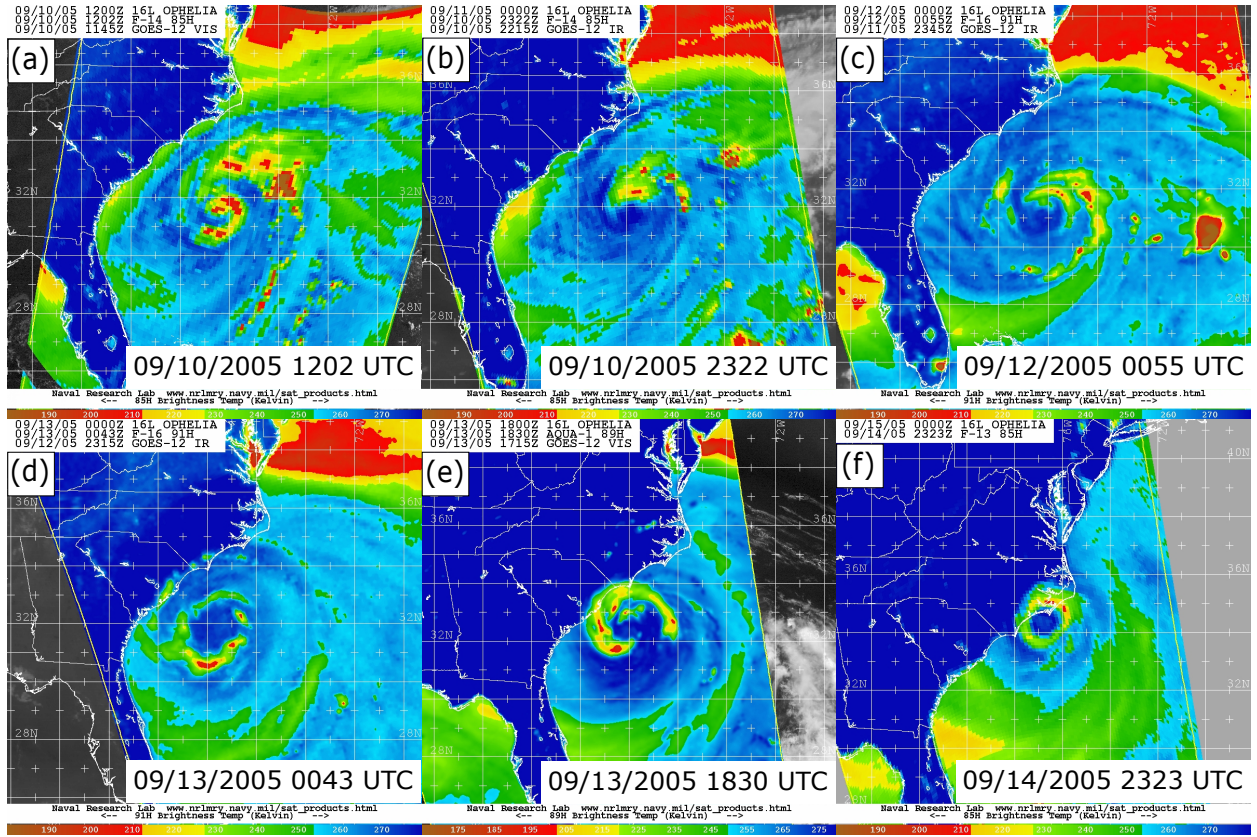


FIG. 6. Satellite microwave brightness temperatures in the ice-scattering channels (horizontally-polarized 85 - 91 GHz) of Hurricane Ophelia as it underwent an eyewall replacement cycle, courtesy of the Naval Research Laboratory.

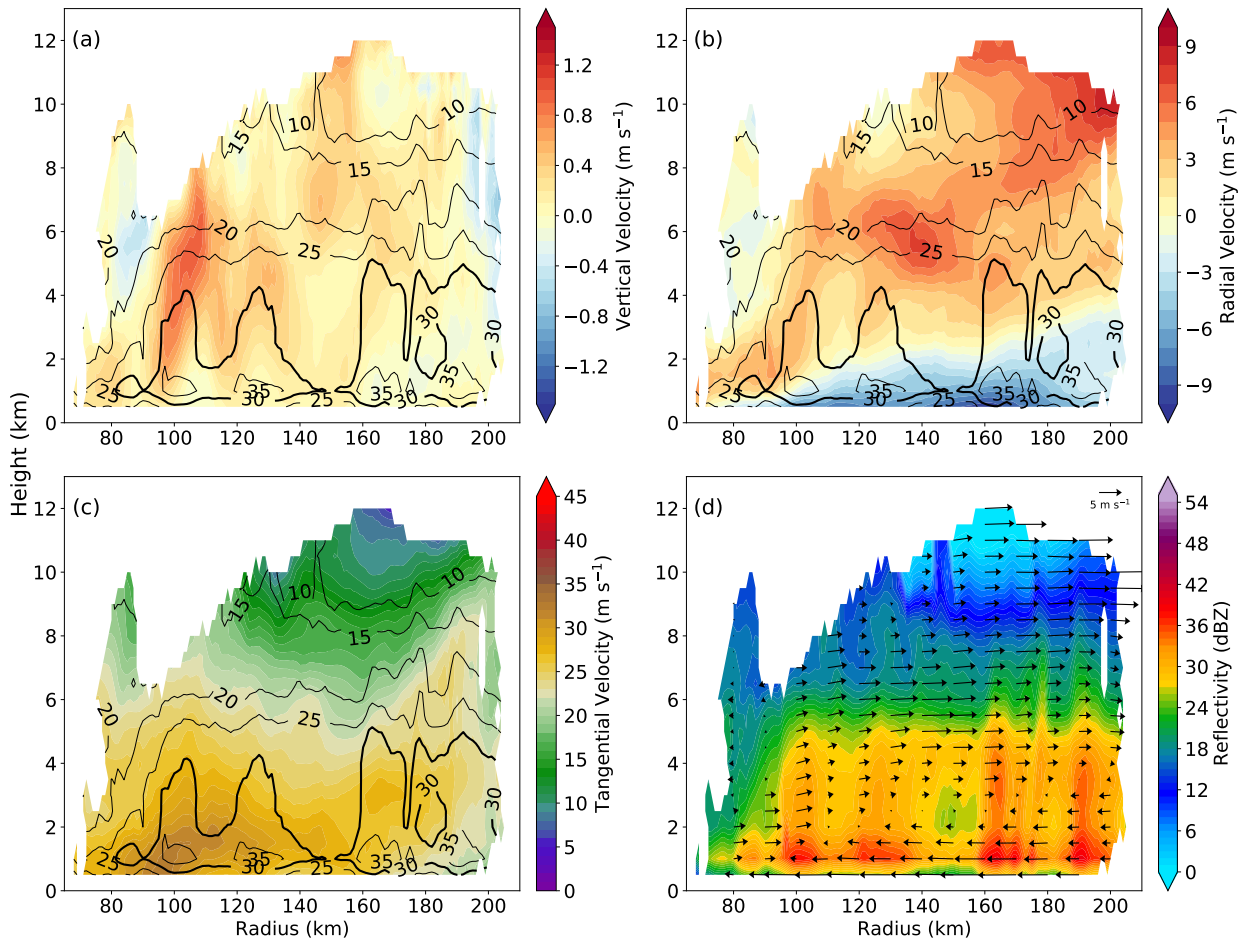


FIG. 7. Sector average (a) vertical, (b) radial and (c) tangential velocities (m s^{-1}) with overlaid contours of sector average reflectivity (dBZ), and (d) the sector average reflectivity (dBZ) with overlaid wind vectors in rainband-C. The 30-dBZ contour is highlighted in (a), (b), and (c) to help distinguish the reflectivity columns (see text).

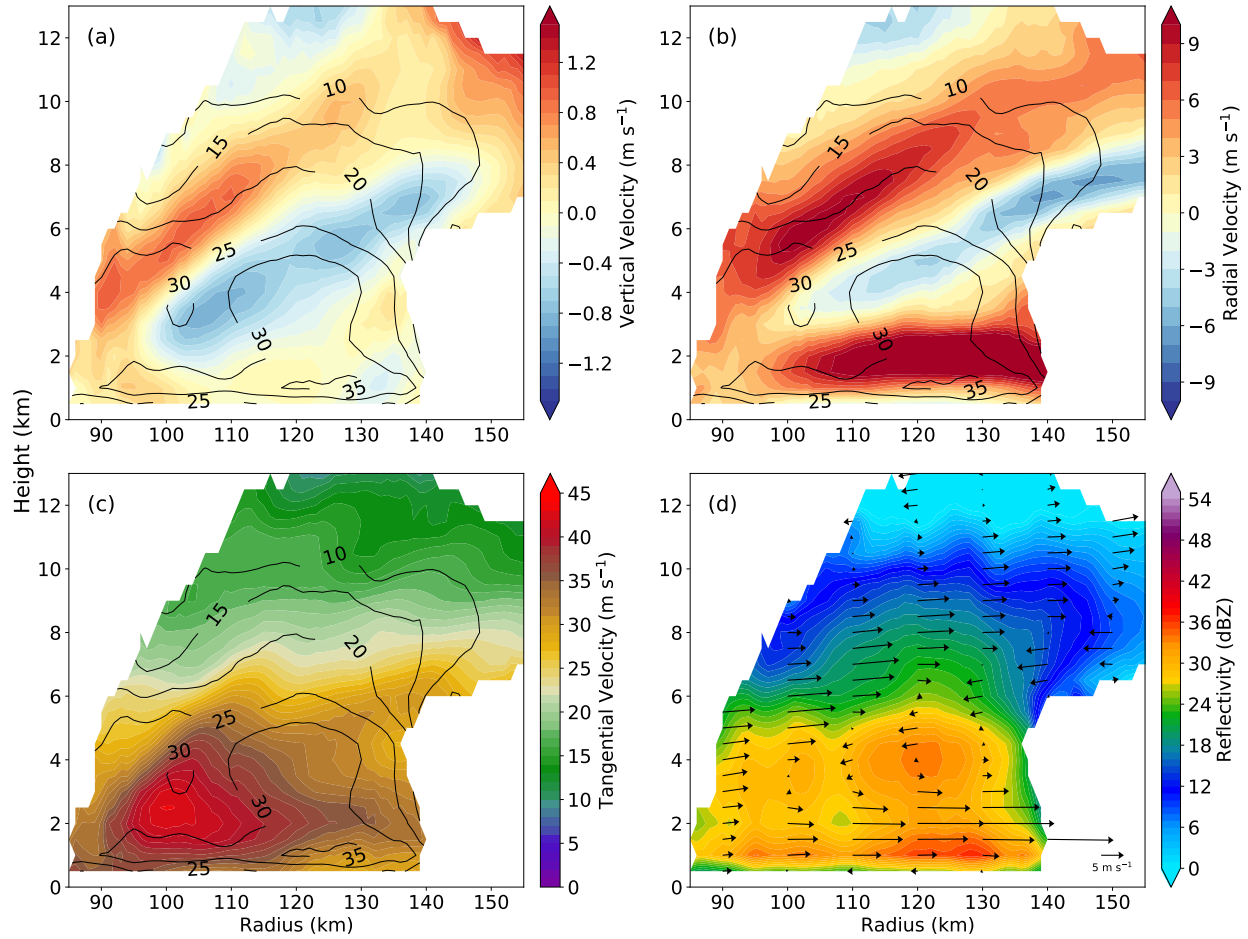


FIG. 8. Sector average (a) vertical, (b) radial and (c) tangential velocities (m s^{-1}) with overlaid contours of sector average reflectivity (dBZ), and (d) the sector average reflectivity (dBZ) with overlaid wind vectors in rainband-S2.

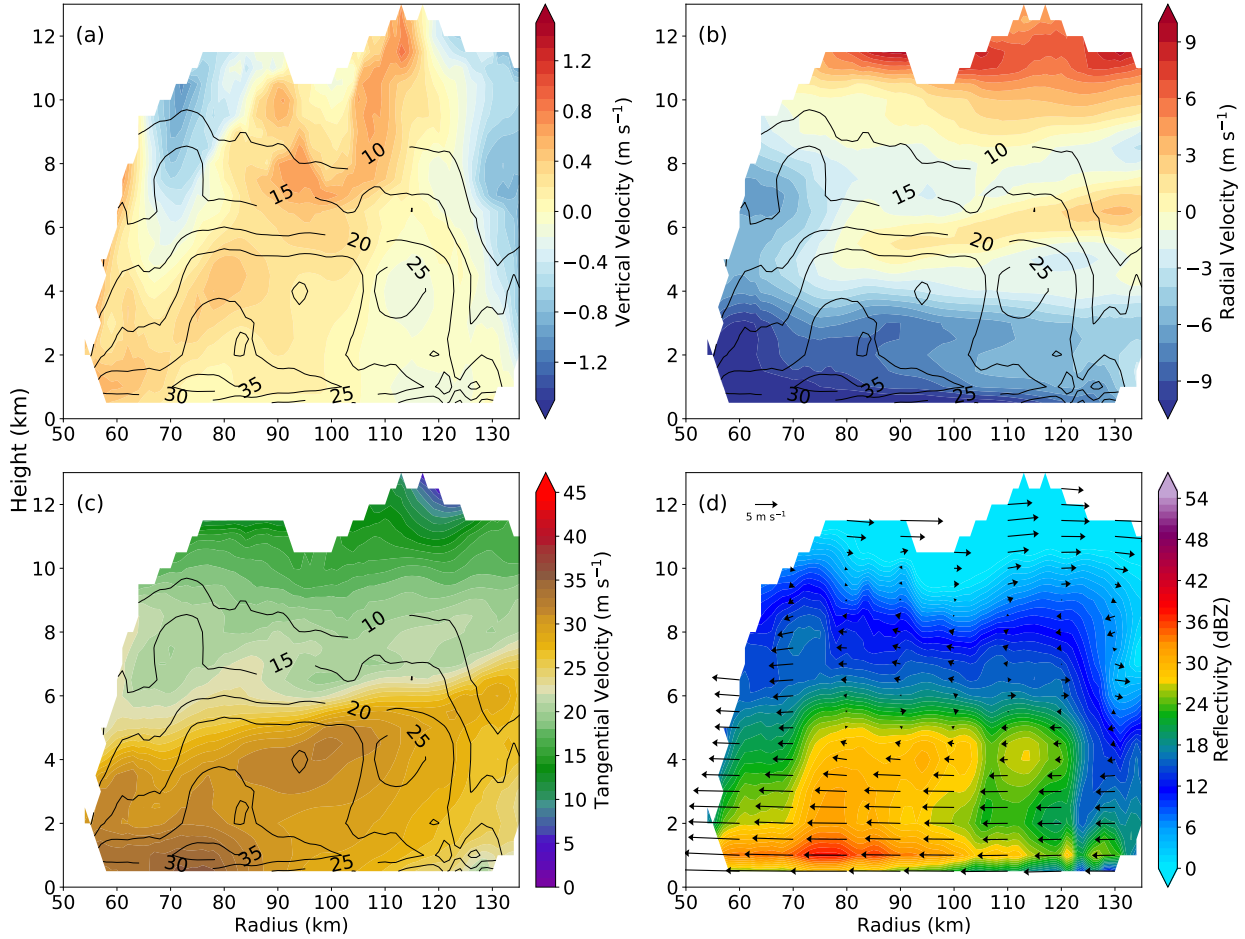


FIG. 9. Sector average (a) vertical, (b) radial and (c) tangential velocities (m s^{-1}) with overlaid contours of sector average reflectivity (dBZ), and (d) the sector average reflectivity (dBZ) with overlaid wind vectors in the developing secondary eyewall (DSE).

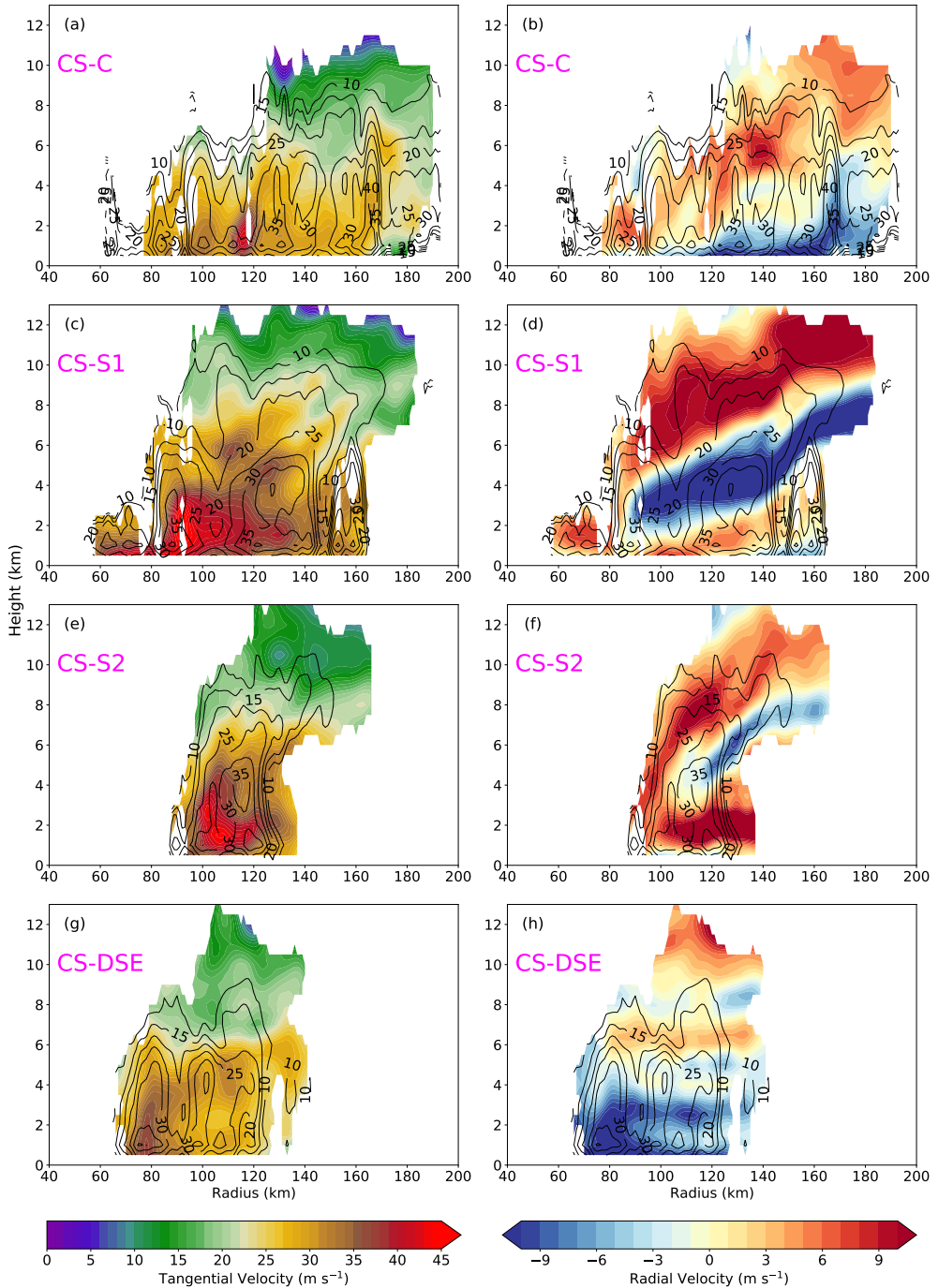


FIG. 10. Individual cross-sections of tangential velocity (m s^{-1}) and radial velocity (m s^{-1}) in each of the rainband sectors where quad-Doppler observations are available. Overlaid are contours of reflectivity (dBZ). The location of the cross-sections (CS) correspond to the lines labeled in Fig. 1a

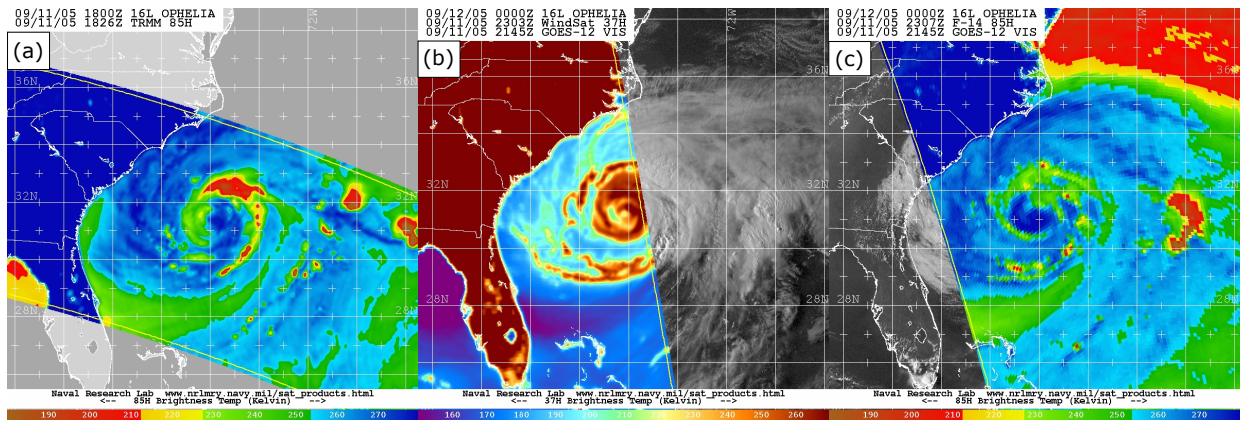


FIG. 11. (a) 85-GHz microwave brightness temperatures of Hurricane Ophelia at the start of the research flights, and (b) 37-GHz and (c) 85-GHz microwave brightness temperatures of Hurricane Ophelia after the conclusion of the research flights on the 11th of September.

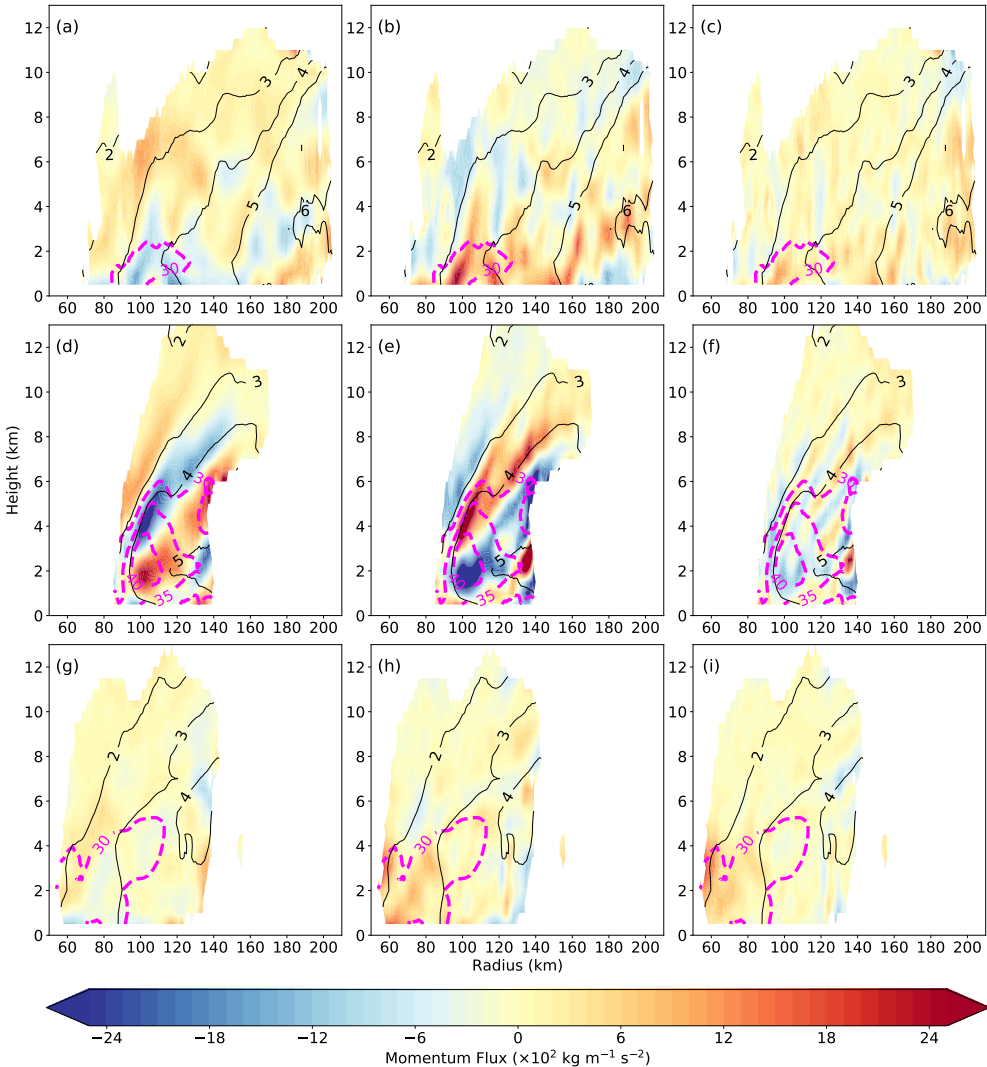


FIG. 12. Vertical flux of absolute angular momentum (left column), radial flux of absolute angular momentum (middle column), and absolute angular momentum tendency (right column) calculated from rainband-C (top), rainband-S2 (middle), and DSE (bottom). Overlaid are contours of sector absolute angular momentum ($\times 10^6 \text{ m}^2 \text{s}^{-1}$; solid black) and contours of 30, 35, and 40 m s^{-1} tangential winds (dashed magenta).

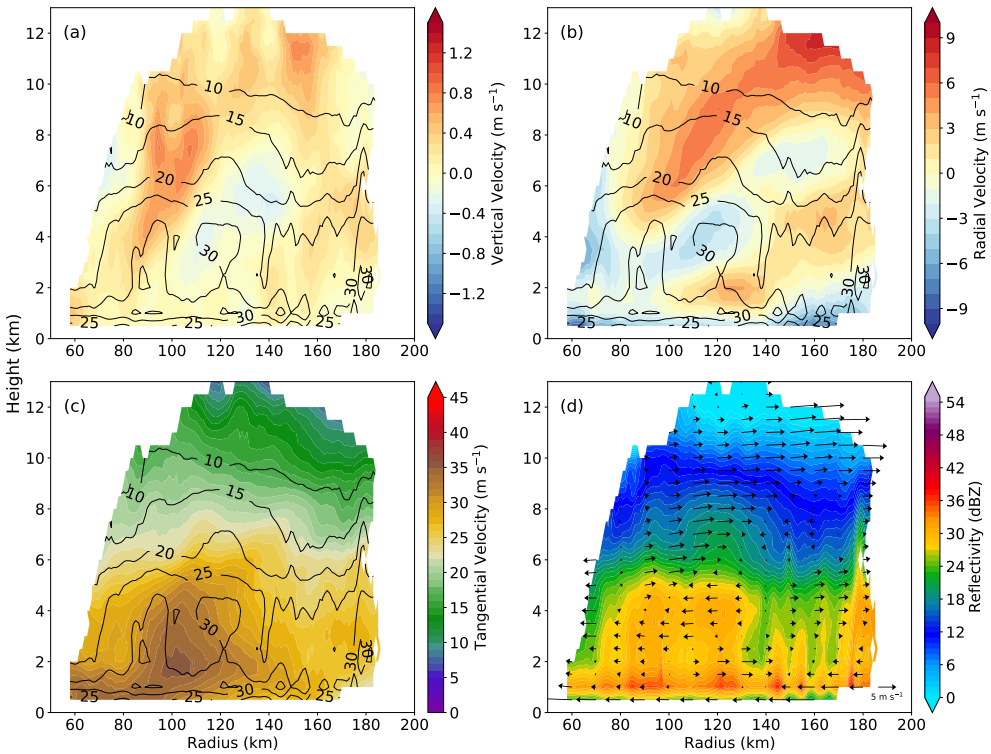


FIG. 13. Axisymmetric (a) vertical, (b) radial and (c) tangential velocities (m s^{-1}) with overlaid contours of axisymmetric reflectivity (dBZ), and (d) the axisymmetric reflectivity (dBZ) with overlaid wind vectors.

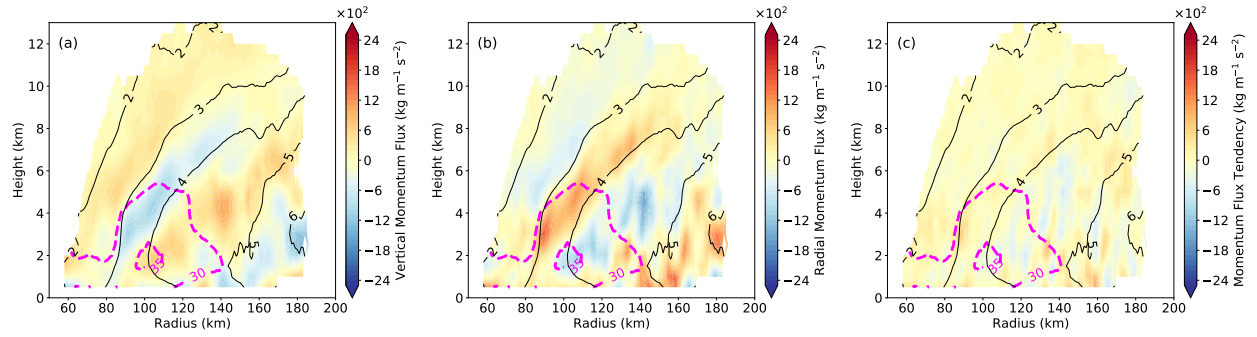


FIG. 14. Axisymmetric vertical flux of absolute angular momentum (left column), radial flux of absolute angular momentum (middle column), and absolute angular momentum tendency (right column). Overlaid are contours of axisymmetric absolute angular momentum ($\times 10^6 \text{ m}^2 \text{s}^{-1}$; solid black) and contours of 30, 35, and 40 m s^{-1} tangential winds (dashed magenta).

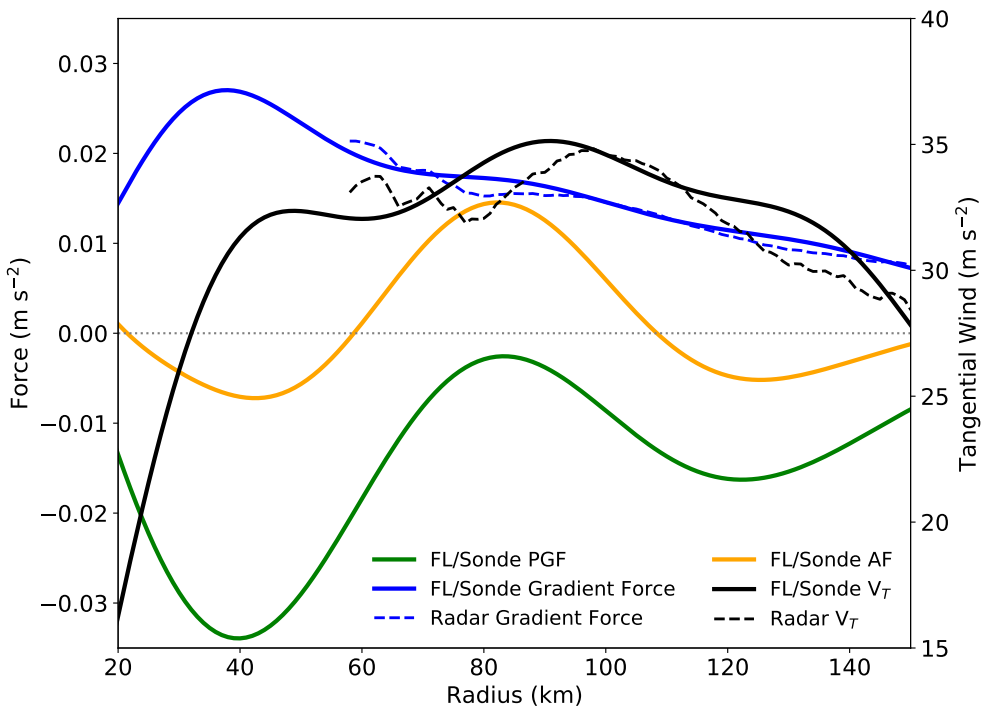


FIG. 15. Radial profiles of agradiant force (yellow line) and its components: (i) pressure gradient force (green line) and (ii) the sum of the centrifugal and Coriolis forces as a “gradient wind force” (blue line). Also included is the axisymmetric tangential winds (black line). All fields are plotted at 1.2 km altitude, with the solid lines denoting fields computed from the axisymmetric SAMURAI analysis using in-situ data, and dotted lines denoting fields computed using the axisymmetric tangential winds from the SAMURAI radar analysis.